

Review

# Molecular Catalysts for OER/ORR in Zn–Air Batteries

Evgeny V. Rebrov<sup>1,2,\*</sup>  and Peng-Zhao Gao<sup>3</sup><sup>1</sup> School of Engineering, University of Warwick, Coventry CV4 7AL, UK<sup>2</sup> Department of Chemical Engineering and Chemistry, Eindhoven University of Technology, P.O. Box 513, 5600 MB Eindhoven, The Netherlands<sup>3</sup> College of Materials Science and Engineering, Hunan University, Changsha 410082, China; gaopengzhao7602@hnu.edu.cn

\* Correspondence: e.rebrov@warwick.ac.uk or e.rebrov@tue.nl

**Abstract:** Zn–air batteries are becoming the promising power source for small electronic devices and electric vehicles. They provide a relatively high specific energy density at relatively low cost. This review presents exciting advances and challenges related to the development of molecular catalysts for cathode reactions in Zn–air batteries. Bifunctional electrocatalysts for oxygen reduction reaction (ORR) and oxygen evolution reaction (OER) play the main role in improving performance of reversible fuel cell and metal–air batteries. The catalyst development strategies are reviewed, along with strategies to enhance catalyst performance by application of magnetic field. Proper design of bifunctional molecular ORR/OER catalysts allows the prolongment of the battery reversibility to a few thousand cycles and reach of energy efficiencies of over 70%.

**Keywords:** Zn–air battery; bifunctional electrocatalyst; ORR; OER; ferromagnetic electrocatalysts; AC magnetic field

## 1. Introduction

In many areas, technologies are changing from fossil fuel technology to electrified technologies that are driven by renewable electrons. Currently these transformations are taking place very rapidly, enabled by novel materials that reduce the cost of renewable electrons and their storage, and extend the range of these novel applications. The increasing role of electricity as an energy carrier in decarbonizing the economy results in a higher demand for electrical energy storage in the form of rechargeable batteries. It remains a great challenge to achieve next-generation rechargeable batteries with high energy density, excellent cycling stability, good rate capability, efficient active material utilization, and high Coulombic efficiency. Two battery applications driving demand growth are: (i) electric vehicles and (ii) stationary forms of energy storage. As renewable electrons become readily available and more cost competitive with conventional energy sources, the breadth of their potential application significantly increases. The solar industry has already achieved the US Department of Energy's original SunShot 2020 cost target of USD 0.06 per kWh for utility-scale photovoltaic solar power [1]. The most recent 700 MW PV facility in Portugal has a bid power cost of USD 0.013 per kWh, which makes this one of the lowest costs of electricity [2]. Yet, the amount of energy storage required in the future is significant. It requires 1.0 TWh of storage to mitigate the intermittency issue and to achieve 90% renewables by 2035 worldwide [3]. Europe is set to host around 280 gigafactories (6000 GWh) by 2030 and the growth is currently driven by automotive demand which is linked to the decarbonization of road transport.

Rechargeable batteries are considered as the primary energy source for future transportation and stationary applications. The growth observed in electric vehicle (EV) adoption is expected to continue due to government incentives for consumers in many markets of the world. Analysts project mobility storage demands in 2030 of 0.8 to 3.0 TWh, with



**Citation:** Rebrov, E.V.; Gao, P.-Z. Molecular Catalysts for OER/ORR in Zn–Air Batteries. *Catalysts* **2023**, *13*, 1289. <https://doi.org/10.3390/catal13091289>

Academic Editor: Carl Redshaw

Received: 25 July 2023

Revised: 28 August 2023

Accepted: 6 September 2023

Published: 10 September 2023



**Copyright:** © 2023 by the authors. Licensee MDPI, Basel, Switzerland. This article is an open access article distributed under the terms and conditions of the Creative Commons Attribution (CC BY) license (<https://creativecommons.org/licenses/by/4.0/>).

the demand for light-duty EVs dominating near-term markets [4]. In today's EV market, lithium-ion batteries (LIBs) are extensively employed [5]. The specific energy of lithium-air batteries is  $5928 \text{ Wh kg}^{-1}$  and a nominal cell voltage is  $2.96 \text{ V}$  [6]. LIBs gain a competitive advantage in terms of stability and energy density and their rather high safety plays a crucial role in empowering the EV industry. However, they suffer from low ionic conductivity at room temperature and advanced functional electrolytes are still in the research stage. The leading manufacturers of LIBs are listed in Table 1.

Owing to its high reactivity, lithium is present only in compounds in nature: either in brines or hard rock minerals. The rarity of lithium in nature results in a rather high price of LIBs. Lithium demand will rise further from approximately 500,000 tons of lithium carbonate equivalent (LCE) in 2021 to some 3 to 4 million tons in 2030 [7]. However, satisfying the demand for lithium is not a trivial problem. Electric vehicle (EV) sales doubled to approximately 7 million units in 2021. At the same time, the Li price increased by 550% in a year [8]. In 2022, the lithium carbonate and lithium hydroxide price passed USD 75,000 and USD 65,000 per ton, respectively (compared with a five-year average of around USD 14,500 per ton) [8].

**Table 1.** Leading producers of rechargeable batteries [9,10].

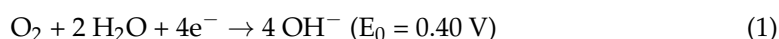
Top 5 Countries/Regions, Share of Commissioned Capacity, 2020 (747 GWh)	Leading Producers	Main Countries in Which Leading Producers Own Battery Manufacturing Plants
China 76% (568 GWh) U.S.A. 8% (60 GWh) Europe 7% (52 GWh) Republic of Korea 5% (37 GWh) Japan 4% (30 GWh)	CATL (Ningde, China)	China (Shenyang) JV "BBA" with BMW Group, Germany (Erfurt)
	BYD (Shenzhen, China)	China (Pingshan in Shenzhen) France, Hungary
	Panasonic (Osaka, Japan)	Japan, China, USA (Nevada)
	LG (Seoul, Republic of Korea)	Republic of Korea (Ochang), China (Nanjing), USA (Holland, Michigan), Poland (Wroclaw)
	Samsung (Suwon, Republic of Korea)	Republic of Korea (Ulsan; Pohang), USA (Auburn Hill), China (Tianjin, Xi'an), Europe (Hungary, Austria), India, Malaysia, Vietnam
	SK Innovation (Seoul, Republic of Korea) Gotion High-Tech (Hefei, China), Envision (Shanghai, China), AESC (Yokohama, Japan)	Republic of Korea (Seosan), China (Changzhou, Jiangsu), USA (Commerce, Georgia; two locations in JV with Ford), Hungary (Komaron, Ivancsá) Japan (Kanagawa); USA (Tennessee), UK (Sunderland) and China (Jiangyin) China (Hefei), Germany (Salzgitter)

Therefore, much research is devoted to alternative batteries based on zinc (Zn) cathodes. They show a large potential for further development as energy storage devices. As competitive electrochemical technologies for energy storage and conversion, rechargeable zinc-based batteries have attracted increasing attention including the zinc-ion battery and zinc-air battery (ZAB) [11]. Compared with the zinc-ion battery, the rechargeable zinc-air battery (ZAB) shows high energy density because of the employment of  $\text{O}_2$  as the active material, low negative potential ( $-0.762 \text{ V}$  vs. SHE), abundance, low toxicity, and intrinsic safety advantages. Rechargeable ZABs are also considered as one of the most economically feasible battery solutions for grid-scale applications [12]. Currently, several companies have already started deploying ZABs for utility scale energy storage, including NantEnergy, who installed 3000 systems in nine countries at a manufacturing cost as low as USD 100 per kWh in 2019 [11]. Large ZABs with a total charge of 500–2000 Ah can be used in railway

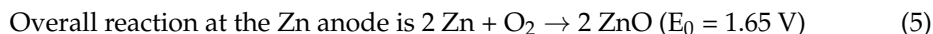
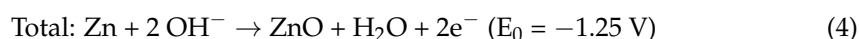
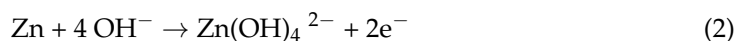
and maritime devices, while small scale batteries with a charge of 200–400 mAh are used for small hearing-aid devices [12].

The average Zn price in 2021 was USD 2950 per ton [13], indicating that this material is ca six times cheaper than lithium carbonate. The volumetric energy density of ZABs is relatively high (6136 Wh L<sup>-1</sup>). Moreover, the currently achievable battery lifetime in practical conditions is around 150 cycles, and the energy efficiency is below 60%, which is still far from the operational requirements of EVs [14]. This is due to excessive dendrite formation on the electrode and electrolyte carbonation. Therefore, further improvements are required to increase energy density, safety, and to decrease costs.

A typical ZAB consists of a porous air cathode and a Zn metal anode, separated by an alkaline electrolyte. During discharge, O<sub>2</sub> from the air permeates the porous cathode and is reduced on the catalyst surface (Figure 1a).



Here  $E_0$  represents the standard electrode potential with respect to the standard hydrogen electrode. At the same time, the Zn anode reacts with hydroxide ions to produce soluble zincate ions as well as insoluble ZnO.



However, the practical working voltages are usually lower than 1.20 V, much less than the theoretical potential (1.65 V) in consideration of the internal loss of battery, resulting from the overpotential over the catalysts, ohmic loss and concentration loss. In addition to these factors, Zn is thermodynamically unstable in alkaline solution as zinc has a higher negative reduction potential than hydrogen, resulting in hydrogen gas evolution at the solid/liquid interface gas:



This reaction deteriorates the efficiency of the Zn anode and accelerates self-discharge. CO<sub>2</sub> from the air also reacts with the alkaline electrolyte to form carbonates (Equations (7) and (8)), that could block the gas diffusion layer to prevent the flow of oxygen.



The mobility of carbonate/bicarbonate anions is lower than that of OH<sup>-</sup> [15], and hence, the carbonation process causes a decline in the ionic conductivity of the alkaline electrolyte.

The charge process is fulfilled by reversing the reactions (Figure 1b). The oxygen-evolution reaction (OER) at the air electrode generates oxygen. Zincate ions are reduced to the Zn(0) at the anode surface. Electrocatalysis plays an important role in nearly all rechargeable battery technologies. Electrocatalysis is one of the main technologies to directly use renewable electrical energy to drive reactions. A SciFinder search on the terms “electrocatalyst” and “rechargeable battery” returned >3700 items for the period 2020–2022, mainly related to the development of novel catalysts for oxygen evolution reaction (OER) and oxygen reduction reaction (ORR), with about 50% of all research papers coming from

China. Developing an exceptional catalyst capable of accelerating both oxygen reduction reaction (ORR) and OER remains challenging.

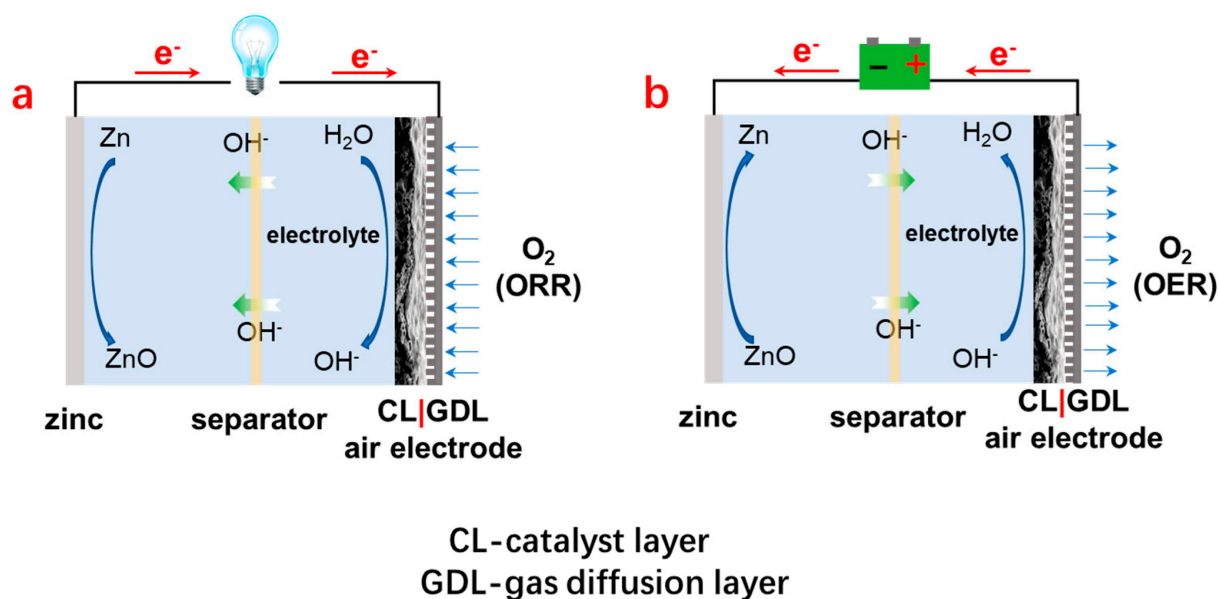


**Figure 1.** The schematic discharging (a) and charging (b) mechanisms of rechargeable zinc-air batteries [16]. During discharge,  $O_2$  from the air permeates the porous catalyst layer (shown with blue arrows) and is reduced on the catalyst surface with water molecules (Equation (1)). The hydroxide ions diffuse via the separator to the zinc electrode (shown with green arrows). During charging, the OER at the air electrode generates oxygen (shown with blue arrows).

Among reported catalysts, single-atom catalysts (SACs) have attracted extensive attention due to their maximum atom utilization efficiency, homogenous active centers, and unique reaction mechanisms. The novel electrocatalysts also encompass metal clusters and bimetallic nanoparticles, and metal catalysts derived from metal organic frameworks (MOFs). Due to the environmental effects of metal usage, many research groups develop metal-free carbon-based catalysts [17]. The use of relatively cheap and electrically conductive carbon supports improves the catalyst dispersion and active area while decreasing the costs. However, despite the advanced methods such as defect engineering (heteroatom doping) to create favorable metal-free carbon-based catalysts, their catalytic activity is insufficient and not yet comparable to metal-based catalysts [17]. As a result, it is impractical to entirely abandon the use of metal materials in building bifunctional catalysts at the current state, highlighting the significance of integrating the advantages of different elements to construct high-performance catalysts to improve the ORR and OER. Several strategies, including structural engineering, defect engineering, and single atom engineering, have been used to develop effective catalysts to improve the electrochemical performance of ZABs. A great deal of research has been devoted to the development of novel air cathodes loaded with bifunctional catalysts, and they can be sorted by their constituents, such as metal oxides and carbon-based materials.

Electrocatalytic reactions may further be improved by employing magnetic heating of composite magnetic catalysts. Local heating of the electrodes was already employed to improve cell performance. However, conventional heating systems cannot avoid global heating of the whole electrochemical cell, and, therefore, inductive heating is often applied. It allows the localization of heating in the immediate vicinity of magnetic nanoparticles (MNPs) when these are positioned in an external AC magnetic field [18]. Magnetic hyperthermia requires the application of magnetic nanoparticles compatible with heterogeneous catalysts, when placed in an alternative magnetic field, to convert the energy into heat. The power generated by the magnetic nanoparticles is governed by their specific absorption rate (SAR). A SAR of above  $1 \text{ kW g}^{-1}$  is required for applications in catalysis, in the range

of frequencies (100–500 kHz) and magnetic fields (20–100 mT) already used in industry. This is a relatively new research area and SciFinder search on the terms “magnetic catalyst” and “inductive heating” returns less than 50 items for the period 2019–2023, mainly related to the development of composite magnetic catalysts.

In this review, we discuss recent advances in the development of nanostructured catalysts, including single atom catalysts on carbon supports, mono and bi-metallic catalysts, mixed metal oxides and layered double hydroxides for ORR and/or OER electrocatalysis, with a focus towards improving their performance in ZABs. Structure–activity relationships in oxygen electrocatalysis are highlighted. Further enhancement of catalytic activity by application of an external magnetic field is also discussed. Finally, the remaining challenges for the application of nanostructured catalysts in ZABs are highlighted. The overall aim is to provide a snapshot over development for ORR and OER electrocatalysis.

## 2. Air Electrode Catalysts

The air cathode has a considerable effect on electrochemical behavior of rechargeable batteries. It is commonly composed of three components: (i) the current collector, (ii) the gas diffusion layer (GDL) and (iii) the catalyst. A binder-free air electrode was formed by deposition of cobalt oxide nanoparticles on a carbon nanofiber mat by thermally treating electrospun Co(II)-containing polyacrylonitrile fibers [19]. The battery exhibited better stability and cycling performance compared with a conventional ZAB assembled with a Pt/C catalyst. Aerosol printing is an emerging additive manufacturing technology which can deposit a catalytic coating on the electrode with high precision, so that the catalyst layer has excellent adhesion with a carbon cloth surface, and interface resistance has little influence on the electrochemical characteristics of the electrode and is suitable for a flexible battery. The technology for preparing the conformal catalytic layer based on the aerosol method was reported to form a catalytic coating on the cathode of the battery [20].

### 2.1. Activated Carbon Materials

Activated carbons (ACs), typically derived from biomass, have gained great interest due to their low price, reproducibility and environmentally friendly nature. Numerous biomass wastes (coconut shells, vegetable wastes, etc.) were used as precursors to prepare ACs with large effective specific surface area. Another considerable advantage of biomass precursors is that they contain rich sources of heteroatoms (e.g., N, P, O, S), which are natural dopants for porous carbon materials. Different oxygen-containing functional groups on the surface of ACs provide active sites for catalytic processes. These electron-withdrawal groups create a positive charge density on adjacent carbon atoms which can facilitate the adsorption of OH<sup>-</sup> ions, promote transportation of electrons and assure easy and rapid recombination of two adsorbed oxygen atoms for OER. The oxygen-containing groups can favor the adsorption of water via hydrogen bonding [21]. The construction of hierarchically porous materials (HPAC) achieves fast ion transportation and provides a larger effective surface area for applications for the OER.

The use of templates makes it easy to create porous catalysts with different morphologies. Nanocasting involves the preparation of templates and the transfer of morphological information from the templates to the ACs. Montmorillonite, copper, halloysite, SiO<sub>2</sub>, and block copolymers are often used as templates. For example, using a block polymer, poly(styrene)-block-poly(ethylene oxide), mesoporous carbon spheres with a large specific surface area of 356 m<sup>2</sup> g<sup>-1</sup> were fabricated [22]. The activation methods of carbon materials are divided into chemical, physical, and combined (chemical–physical) methods. Among them, physical activation has the advantages of low cost and low environmental impact. Usually, the ACs activated by water vapor have a wide pore size distribution (PSD) due to the faster evaporation rate and the smaller diameter of water molecules. The ACs activated by CO<sub>2</sub> have a relatively narrow PSD due to the slower diffusion rate and large diameter of CO<sub>2</sub> molecules [23].

The heteroatom incorporated into ACs is advantageous to regulate their electron donor performance and, thus, adjust the electrical and chemical performance of their surface. Nitrogen (N), sulfur (S), oxygen (O), boron (B), and phosphorus (P) -doped ACs were investigated [24]. The synergistic effect of multiple-heteroatoms-doped ACs on the electrochemical properties was reported. Various N- and S-doped ACs with a low S content were obtained by pyrolysis of protic ionic liquids (PILs) of  $[R-NH_x][HSO_4]$  (R means carbon chain) [25].

The N-doped HPACs enhance both electronic conductivity and surface wettability and, therefore, they are considered as ideal electrode materials. The presence of nitrogen heteroatoms in hexagonal carbon rings raises the basicity, electrical conductivity, and oxidation resistance of ACs. The N-doped HPACs are typically produced by pyrolysis of polyacrylonitrile, polyaniline, phenolic resin, and biomass derivatives [20]. Nitrogen-doped carbon nanotube supported metal catalysts (M-N-C, M=Fe, Co) decrease the binding energies of the surface-adsorbed  $*OOH$  and  $*OH$  species, thus boosting the catalytic activity in the ORR reaction. Yet many carbon supports suffer from serious degradation under high potentials of OER process [26]. The potential above 0.207 V may already result in the oxidation of ACs to  $CO_2$ . This process is accelerated when a noticeable amount of oxygen is generated at a potential of 1.5 V [27]. The electrochemical stability of ACs is highly dependent on their morphology, structure, and dopants. For instance, amorphous carbon black is highly unstable, whereas highly graphitized carbon nanotubes can significantly improve their stability under OER conditions. However, N-doped graphene remains expensive, complex to set up, and difficult to scale up for practical applications. Chemical vapor deposition (CVD) for graphene synthesis requires metal substrates such as nickel or copper as the growth catalyst.

Extremely rapid heating for the synthesis of highly open structured N-doped graphene sheets (N-ex-G) was demonstrated [28]. The N-ex-G were produced by fast heating ( $>150\text{ K s}^{-1}$ ) to  $1100\text{ }^\circ\text{C}$  under an Ar/ $NH_3$  flow. The materials exhibited hexagonal symmetry with the existence of symmetrical three-fold  $sp^2$ -bonding of carbon atoms with pyridinic N, pyrrolic N, and quaternary N atoms. The N-ex-G nanosheets showed very comparable ORR activity to that of a commercial Pt/C catalyst. The respective ZAB with N-ex-G demonstrated a current density of  $47.6\text{ mA cm}^{-2}$  at 0.8 V and a power density of  $42.4\text{ mW cm}^{-2}$ .

The graphene/metal oxide composites combine the excellent conductivity of graphene and the high energy density of transition metal oxide [29]. Graphene oxide (GO) is mostly used as a precursor for preparing graphene/metal oxide composites, and it is mixed with a transition metal compound, then the transition metal oxide is generated in-situ on the surface of the graphene oxide by methods such as coprecipitation, hydrothermal or solvothermal synthesis.

Metal organic frameworks (MOFs), wherein transition metals are coordinated by organic ligands in a 3D network, are excellent precursors for the synthesis of porous carbon- or nitrogen-doped carbon architectures and modified porous carbon materials. MOFs are also an important platform material in the area of bifunctional ORR/OER electrocatalysts. For example, zeolitic imidazole framework-67 (ZIF-67) has been extensively employed for the synthesis of porous  $Co_4N/Co-N_x-C$  composites. Upon carbonization under  $N_2$  atmosphere,  $Co-N_x-C$  nanocomposites that partially inherited the porous framework were formed (Figure 2).

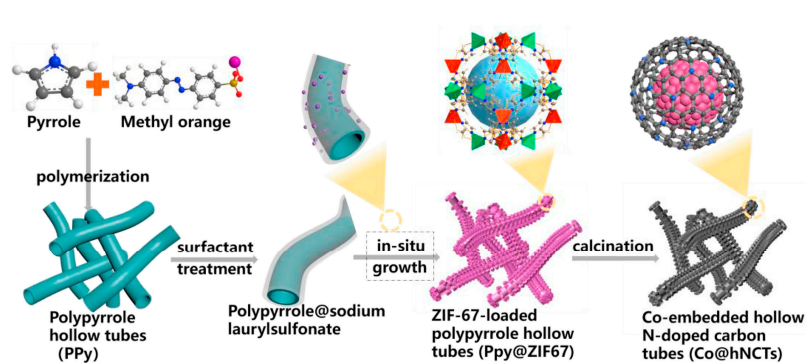


**Figure 2.** Schematic illustration of the synthesis of MOF-derived Co@hNCT catalysts. Adopted from [30].

A MOF-derived synthesis method was recently patented for an Fe-Eu-MOF/GO bimetallic cathode catalyst [31]. The prepared catalyst demonstrated a higher activity in both ORR and OER reactions and very high stability as compared with respective monometallic catalysts due to a large number of oxygen vacancies that enhance the interaction between metal nanoparticles and their support; in addition, they enhance the adsorption of oxygen on the surface of the catalyst and enable electrons to be rapidly transferred in an electrochemical reaction.

## 2.2. Monometallic Catalysts

The rates of ORR and OER in rechargeable batteries are relatively slow and they require different catalysts because of their different mechanisms onto the catalyst surface. Therefore, bifunctional electrocatalysts are needed for the best performances. The noble metal catalysts have high conductivity, high catalytic performance and good stability. The Pt-based nanocomposites are used for ORR [32]. However, the formation of irreversible Pt=O decreases its catalytic activity toward OER. On the contrary, IrO<sub>2</sub> and RuO<sub>2</sub> are effective for OER but not as active for ORR [33,34]. Yet, noble metal catalysts are costly, which limits their large-scale application. Therefore, the goal of catalyst development, including for Pt and other precious metal-based catalysts, is to increase the total number and/or the intrinsic activity of active sites [35]. This goal can be achieved by several strategies, which are summarized in Figure 3.

Nonprecious bifunctional electrocatalysts with low cost and efficient catalytic activities in ORR and OER are highly desired to promote the commercialization of ZABs. From the perspective of elemental composition, Fe and Ni have been paid much attention as the promising earth-abundant transition metals for the design of OER catalysts, especially Ni/Fe-based micro/nanostructures as a new generation of catalytical materials (such as metal hydroxide and mixed-metal oxides) which were developed over the last few years. They have attracted extensive attention because of their facile synthesis [36]. A gram of IrO<sub>2</sub> (99 wt %) and RuO<sub>2</sub> (99.5 wt %) costs ca USD 43 and USD 95, respectively. The price of iron oxide and nickel oxide with a 99 wt % purity is 50–100 times lower. Therefore, these transition metal-based compounds are appealing candidates, especially for bifunctional catalysts [37,38]. In comparison with precious metals, they offer advantages of low prices and greater availability. Cobalt oxides, and Co-perovskites exhibit high intrinsic catalytic activity for OER in alkaline media (Table 2). However, their apparent activity is limited by either poor electronic conductivity or low surface area. Their durability is also limited by their tendency of sintering and/or aggregation. In alkaline solutions, corrosion limits the effective lifetime of Fe- and Ni-based OER electrocatalysts. Typically, monometallic Fe-based compounds on various substrates in a 1 M KOH aqueous solution with a constant overpotential were active for less than 180 h due to corrosion. Although the initial decay of a catalyst sometimes could increase the active surface area and catalytic activity, catalyst activity always reduces in the long-term.

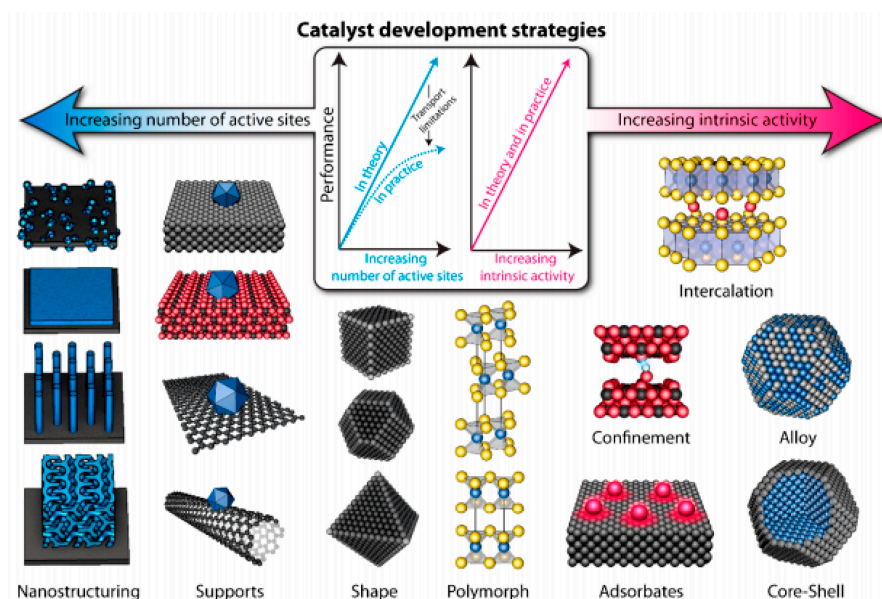


**Figure 3.** Different development strategies for metal catalyst preparation. Schematic of various catalyst development strategies, which aim to increase the number of active sites and/or increase the intrinsic activity of each active site. Adopted from [36].

**Table 2.** Recent advances in bifunctional MOF-derived catalysts.

Catalyst	OCV (V)	PPD (mW cm <sup>-2</sup> )	Discharge-Charge Voltage Gap (V) at Current Density	Cycling Stability	Ref
HCo@FeCo/N/C	1.45	125	0.84 (10 mA cm <sup>-2</sup> )	200 h (10 mA cm <sup>-2</sup> )	[39]
Co@N-CNT hollow nitrogen-doped carbon nanotubes	1.45	149	0.85 (5 mA cm <sup>-2</sup> )	500 h (5 mA cm <sup>-2</sup> )	[30]
Co/N-doped CNT/graphene hybrid	1.48	253	0.76 (5 mA cm <sup>-2</sup> )	9000 cycles, 3000 h (5 mA cm <sup>-2</sup> )	[40]
ZIF-derived Co <sub>9</sub> S <sub>8</sub> /GN graphene nanosheet		186	0.52 (2 mA cm <sup>-2</sup> )	2000 cycles, 147 h (2 mA cm <sup>-2</sup> )	[41]
CoP/(N,P) codoped porous carbon	1.4	186	1.00 (2 mA cm <sup>-2</sup> )	80 h (2 mA cm <sup>-2</sup> )	[42]
Ni-Co-S/(N,S) codoped porous carbon	1.43	137	0.73 (10 mA cm <sup>-2</sup> )	180 cycles (10 mA cm <sup>-2</sup> )	[43]
Co@SiO <sub>x</sub> /N-doped carbon		138	0.82 (5 mA cm <sup>-2</sup> )	400 h (5 mA cm <sup>-2</sup> )	[44]
Co/Co <sub>9</sub> S <sub>8</sub> @CNT	1.44	185	0.75 (5 mA cm <sup>-2</sup> )	50 cycles, 2000 h (5 mA cm <sup>-2</sup> )	[45]
Ba <sub>0.5</sub> Sr <sub>0.5</sub> Co <sub>0.8</sub> Fe <sub>0.2</sub> O <sub>3</sub>			0.83 (5 mA cm <sup>-2</sup> )	1800 cycles, 300 h (5 mA cm <sup>-2</sup> )	[46]
Co-MOF/LaCoO <sub>3-δ</sub> hybrid	1.44	126	0.67 (5 mA cm <sup>-2</sup> )	120 h (5 mA cm <sup>-2</sup> )	[47]
Ni <sub>3</sub> Fe/Co-N-C	1.39	68	0.75 (10 mA cm <sup>-2</sup> )	65 h (10 mA cm <sup>-2</sup> )	[48]
Co-NCS@nCNT	1.42	90	0.89 (5 mA cm <sup>-2</sup> )	480 cycles, 80 h (5 mA cm <sup>-2</sup> )	[49]
Co <sub>3</sub> O <sub>4</sub> /Co@NC	1.5	124	0.94 (10 mA cm <sup>-2</sup> )	3600 cycles, 600 h (10 mA cm <sup>-2</sup> )	[50]

These challenges are resolved by anchoring transition metal oxide/nitride nanoparticles into a porous substrate. Anchoring provides sufficient electronic conductivity to enhance charge transfer and greatly increase the dispersion of metal oxides in order to increase the number of active sites and to suppress the sintering of the individual nanoparticles. Furthermore, the doping of N heteroatoms in the carbon lattice enhances the ORR activity. The presence of transition metals (Fe, Co, Ni, Mn) or their alloys can also significantly improve the stability of the nitrogen-doped graphene nanotubes. Different bifunctional electrocatalysts with high activity and durability for both ORR and OER have been developed. Some of them are listed in Table 2.

Transition metals contain partially filled d-orbitals, conferring their compounds with a high electrochemical activity. However, most of them have good OER activity but weak ORR activity. Manganese or mixed cobalt oxides (Mn<sub>3</sub>O<sub>4</sub>, NiCo<sub>2</sub>O<sub>4</sub>) effectively catalyze the ORR because of the variable valence states and coordination structures [51–53]. Co spinel catalysts are the most used among those potential bifunctional electrocatalysts. NiCo<sub>2</sub>O<sub>4</sub>

was synthesized with various structures such as nanosphere, nanosheet and nanorods [54]. These hollow porous structures provide a larger specific surface area as compared with bulk samples of the same materials. The main synthetic methods for nanotube structures are template and electrospinning. The materials prepared by electrospinning have greater brittleness, while the catalysts prepared by the template method have surfactants residues, which reduce the rate of electrocatalytic reactions. In a relatively new approach, a  $\text{Co}_3\text{O}_4$  catalyst was immobilized on a Ni foam by a spray pyrolysis method [55]. The respective ZAB showed an excellent cycling stability of more than 500 charge–discharge cycles at a current density of  $5 \text{ mA cm}^{-2}$ .

Manganese oxides are a specific example of the particularly active catalysts for use with the air electrode for commercialization of primary ZABs due to their rich oxidation states, chemical compositions and crystal structures. The electrochemical activity of  $\text{MnO}_2$ -based catalysts depends on their shape and crystallinity and crystallographic properties (phase composition and crystal size), which can be controlled via synthesis parameters [56]. Many theoretical investigations indicated the roles of oxygen vacancies on  $\text{MnO}_2$  during the ORR in terms of electronic properties. The large variation in the structural disorder of  $\text{MnO}_2$  and, therefore, in internal resistance at the electrode–electrolyte interface limits large-scale applications of this material. Various methods were studied for the preparation of  $\text{MnO}_2$ -based catalysts, such as sol-gel, rheological phase reaction, microemulsion, coprecipitation, solid-state template, microwave and hydrothermal synthesis. Often the density functional theory (DFT) was employed to investigate the effect of oxygen vacancies (OV) on the electrocatalytic performance of  $\text{MnO}_2$ . Defect-engineering of  $\alpha$ - $\text{MnO}_2$  (211) and  $\beta$ - $\text{MnO}_2$  (110) by oxygen vacancy was studied to enhance its catalytic performance [57]. For example, Li et al. studied the electronic properties of OV  $\beta$ - $\text{MnO}_2$  (110), in which the oxygen vacancy in the sub-lattice of the surface structure was purposed [58]. Other DFT results involving the effects of OV on the electronic conductivity of  $\text{MnO}_2$  were systematically examined in the bulk structure and discussed based on the density of states [59,60]. It was shown that the  $\alpha$ - $\text{MnO}_2$  exhibits superior catalytic performance for OER (overpotential of 0.45 V at  $50 \text{ mA cm}^{-2}$ ).

Doping of various quantities of metals into the  $\text{MnO}_2$  lattice often improves the OER catalytic activity. The doping of 0.2 mol% of Ni to  $\alpha$ - $\text{MnO}_2$  reduces overpotential in a 0.1 M KOH to 0.44 V at a  $10 \text{ mA cm}^{-2}$  current density [61]. The surface of the bare  $\text{MnO}_2$  materials has inactive  $\text{Mn}^{4+}$  centers. After doping with Ni, a major part of surface Mn ions reduces to lower oxidation states. The presence of Ni ions results in an electron transfer to the  $\text{Mn}^{4+}$  ions, which creates a distortion in the Mn–O octahedral units and increases OER activity. The incorporation of Ag into  $\alpha$ - $\text{MnO}_2$  improves electrical conductivity and increases the number of oxygen vacancies that also create a considerable distortion in the Mn–O octahedra [62]. As a result, the Ag/ $\alpha$ - $\text{MnO}_2$  catalyst shows a threefold enhancement in current density in OER as compared with the undoped  $\alpha$ - $\text{MnO}_2$  catalyst. The Ag/ $\text{MnO}_2$  demonstrates a power density of  $273 \text{ mW cm}^{-2}$  and maintains a stable performance over 3200 cycles. It can be said that doping transition metal ions into less-active oxide surfaces could create a new avenue for OER mixed metal oxide research.

On the other side, isolated single atom catalysts (SACs) coordinated with nitrogen on a carbon support such as graphene, porous carbon (M-N-C) or on metal oxides have promising perspectives for replacement of precious metal catalysts. In particular, graphitic and diamond carbons show improved resistance to corrosion [63]. Their thermal stability, electronic properties, and catalytic activities can be controlled via interactions between the single atom center and neighboring heteroatoms such as nitrogen, oxygen, and sulfur [64]. The preparation of SACs requires a smaller amount of metal precursors, which relieves the metal availability issues. In general, SACs show higher specific catalytic activity (turnover frequency) as compared with conventional catalysts due to their high dispersion, which is close to 100%, as well as their increased stability. While SACs are still in the early stages of commercialization, their potential for improving catalytic activity and selectivity make them an exciting area of research and development. The market for SACs is fast developing,

as the technology is relatively new and there are still many challenges that need to be addressed before these catalysts can be widely adopted. However, there is growing interest in SACs due to their high catalytic activity, selectivity, and stability. According to a recent report by Markets and Markets, the global market for SACs is expected to grow from USD 334.2 million in 2020 to USD 1.1 billion by 2025, at an annual growth rate of 26% [65].

Currently, Fe-N-C catalysts are considered to be among the most important ORR catalysts due to their hierarchical pores, oriented mesopores and high conductivity (Table 3) [66]. Their ORR catalytic activity is above that of non-noble-metal catalysts and is similar to that of a commercial Pt/C catalyst (Figure 4). In addition, Fe-N-C catalysts have a high stability. The intrinsic ORR activity of the Fe-N<sub>4</sub> sites relates to the electronic structure of carbon supports. However, the origin of ORR activity on Fe-N-C catalysts remains unclear, which hinders the further improvement of their catalytic properties. Several authors have reported that the electronic structure of carbon supports (electron-withdrawing or donating property) affects the d-band center or d-orbital level of the Fe site [67,68]. In their density functional theory (DFT) calculations, Liu et al. studied 42 types of divacancy defects around the Fe-N<sub>4</sub> active site by selectively removing C-C bonds or by rotating the different C-C bonds [69]. They established a relationship between the geometric, electronic structure, and ORR activity of the Fe-N<sub>4</sub> site. The first electron transfer step ( $*O_2 + H^+ + e \rightarrow *OOH$ ) was found to be the potential-determining step (PDS) on all Fe-N<sub>4</sub> configurations. The Fe-O bond length is an important descriptor, which influences the ORR activity. At larger distance between atoms in the Fe-O bond, hybridization between Fe 3d<sub>z<sup>2</sup></sub> and O<sub>2</sub> 2p<sub>z</sub> orbitals results in the activation of O<sub>2</sub>. However, at shorter interatomic distance, the activation of O<sub>2</sub> occurs by the hybridization of Fe 3d<sub>yz</sub> and 2p<sub>y</sub> orbitals. Thus, the hybridization between Fe 3d<sub>z<sup>2</sup></sub>, 3d<sub>yz</sub> and O<sub>2</sub> π\* orbitals is considered to be the origin of high activity of Fe-N<sub>4</sub> sites embedded in the graphene framework [69].

Further improvements are expected through the better understanding of the chemical origin of active sites on Fe-N-C catalysts [70].

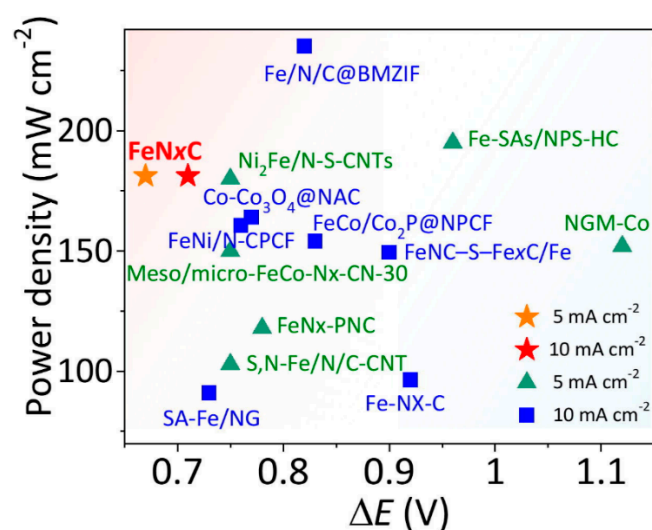


**Figure 4.** Comparison of ORR performance and ZAB performance (voltage gap, V) over different Fe-N-C electrocatalysts. Adopted from [71].

Despite the obvious advantages of Fe-N-C catalysts, their fabrication involves multi-step synthesis and lengthy post-processing procedures which make it difficult to scale up to industrial level. Moreover, the process requires the introduction of metal oxide nanoparticles which may also introduce some impurities decreasing the atom utilization efficiency and reducing catalyst performance. Therefore, developing cost-effective methods for preparation of high-purity Fe-N-C catalysts remains an important task to facilitate their large-scale application. Recently a one-pot synthesis was proposed, which provided a high density of the ORR active site and also facilitated the kinetics [71]. Fe-N-doped

carbon (Fe-NC) was prepared via a pyrolysis of a mixture of glucose and dicyandiamide as carbon source and nitrogen source, respectively, with addition of FeCl<sub>2</sub> and FeCl<sub>3</sub>. The pyrolysis was initially performed in a flow of Ar at 550 °C for 6 h and then at 900 °C for 3 h. The homogenous ink of as-prepared catalyst was used for preparing a ZAB cathode. The ZAB delivered a maximum power density of 181 mW cm<sup>-2</sup> and a voltage gap between discharging and charging of 0.7 V at 10 mA cm<sup>-2</sup>. The ZAB of Fe-N-C runs stably for more than 8 h at 1 mA cm<sup>-2</sup>, and a 0.7 V voltage gap. No changes were observed in the structural, morphological and compositional properties after the reaction, suggesting that the Fe-N-C electrocatalyst is stable in alkaline solutions.

**Table 3.** Performance of ZABs using carbon-based single atom catalysts.

Air Electrode Catalyst	Active Material	Max Power Density (mW cm <sup>-2</sup> )	Specific Capacity (mAh g <sup>-1</sup> )	Duration of Tests (h)	Ref
Fe/N-C	FeN <sub>4</sub> embedded in N-doped carbon.	225	636	260	[72]
Fe-NCCs	Atomic Fe-N <sub>x</sub> dispersed in carbon.	66	705	67	[73]
FeN <sub>x</sub> -PNC	FeN <sub>x</sub> on 2D N-doped carbon.	278	n/a	40	[74]
SA-Fe/NG	Fe-pyrrolic-N species on N-doped carbon.	91	n/a	20	[75]
Co/GO	Atomically dispersed Co on GO.	225	795	50	[76]
Zn/CoN-C	Zn and Co atoms coordinated via N on carbon.	230	n/a	28	[77]

n/a = not available.

Long-term catalyst stability remains a key factor hindering SACs in ZAB applications. Single metal atom centers may be dissolved or they can aggregate to form larger nanoparticles in the course of electrocatalytic reactions, resulting in a significant activity loss due to the sharp reduction in the number of active sites. The undesirable Fenton reaction (Equation (9)) occurs over Fe-N-C catalysts during ORR resulting in hydroxyl radical formation that is detrimental to both the metal sites and the carbon support.



The coordination of S, Se, or P metal atoms is a possible strategy to prevent unwanted side reactions, thus enhancing the stability of SACs without major loss of catalytic activity. Advanced support materials with high conductivity, corrosion resistance, and ability to support SACs at high metal loadings are highly desired. The scale-up process for the synthesis of SACs remains a challenge which limits their adoption by the market of low metal loading, leading to restrictions on a broader range of applications.

Overall, monometallic catalysts demonstrate unsatisfactory bifunctional performance. As discussed above, one of the well-known spinel materials, Co<sub>3</sub>O<sub>4</sub>, has also been studied for decades as a highly efficient and corrosion resistant OER catalyst, but its ORR activity is generally poor. Precise control of catalytic activity by varying the composition of these single metal catalysts remains a difficult task. Therefore, bi- and multi-metallic oxides attract a large interest. Many recent efforts have been made to design and prepare low-cost bifunctional catalysts to catalyze both the ORR and OER with high efficiency and long-term durability.

### 2.3. Mixed Metal Oxide Catalysts

Multicomponent spinel metal oxide nanocomposites demonstrate higher activity in OER as compared with their individual oxides [78]. The improved catalytic performance of spinel oxides is attributed to the presence of both tetrahedral (T<sub>d</sub>) and octahedral (O<sub>h</sub>) transition metal cation sites in these catalysts. Yet this complex structure with multiple sites also presents a significant challenge in identifying the precise OER active sites. For example, NiFe-, CoFe-, and NiCoFe-mixed metal oxides such as spinel NiFe<sub>2</sub>O<sub>4</sub> and

$\text{CoFe}_2\text{O}_4$  are highly active for the OER. Incorporating other metals, such as W into the CoFe-mixed oxides, further enhances the OER activity [79]. It is also known that manganese, cobalt and nickel mixed oxides such as  $\text{Mn}_3\text{O}_4$ ,  $\text{Co}_3\text{O}_4$ ,  $\text{NiCo}_2\text{O}_4$  and  $\text{MnCo}_2\text{O}_4$  could effectively catalyze the ORR in alkaline solutions because of the variable valence states and coordination structures [80]. Liang et al. reported that the oxygen reduction strongly coupled with  $\text{Co}^{\text{III}}/\text{Co}^{\text{II}}$  redox reaction [81]. Other elements such as V, Cr, and Ni, were also studied to enhance the stabilization energy of high-entropy oxides and to tune the subtle relationship between surface electronic properties and catalytic activities. In general, the synthesis temperature, annealing time and temperature, as well as support type, have significant effects on the ORR performance.

Xu et al. obtained novel hybrid materials composed of  $\text{La}_2\text{O}_3$  and  $\text{Co}_3\text{O}_4$  supported on carbon-supported  $\text{MnO}_2$  nanotubes ( $\text{La}_2\text{O}_3/\text{Co}_3\text{O}_4/\text{MnO}_2$ -CNTs) to assemble the air electrode for ZABs [82]. The hybrid catalyst was prepared by dissolving La nitrate and Co nitrate in an ammonia solution with an addition of  $\text{MnO}_2$  nanotubes and CNTs. The mixture was sealed and maintained at  $150\text{ }^\circ\text{C}$  for 6 h in an autoclave, then washed and calcined in air at  $300\text{ }^\circ\text{C}$  for 1 h. The authors suggested that the high catalytic activity was due to formation of new active phases from inorganic materials and their intimacy with the underlying CNT network. The ZAB exhibits a small voltage gap, high reversibility and high stability, suggesting this battery can be used as a power source for portable electronics and in electrical vehicles. The voltage gap of charge/discharge increased by 0.1 V after 543 cycles at  $10\text{ mA cm}^{-2}$ .

Morphological alterations and structural engineering can further boost catalytic performance by enriching the active sites and improving conductivity. A bifunctional catalyst with a narrow half-wave potential of 0.80 V for ORR and a potential of 1.58 V at  $10\text{ mA cm}^{-2}$  for OER, was obtained by embedding of  $\text{NiCo}_2\text{O}_4$  nanowhiskers (NCO) into a 3D honeycombed hierarchical porous N, O-codoped carbon (HHPC) [83] (Figure 5). The support was derived from gelatin biomass via a hard template-activator assisted pyrolysis. The large surface area provided enough space for dispersing  $\text{NiCo}_2\text{O}_4$  evenly to expose abundant ORR and OER active sites. Grain-boundary strength between HHPC and  $\text{NiCo}_2\text{O}_4$  nanowhiskers helped to stabilize the porous carbon network and protect it from corrosion.

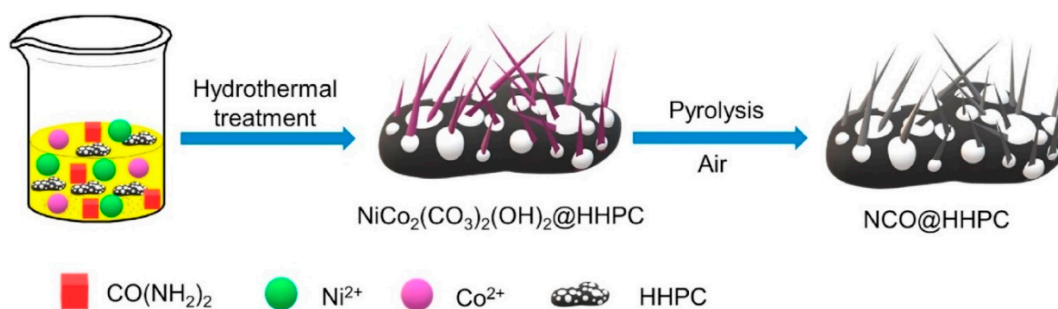


**Figure 5.** Schematic synthesis process of  $\text{NiCo}_2\text{O}_4$  nanowhiskers (NCO) into biomass-derived honeycombed hierarchical porous N, O-codoped carbon. Adopted from [83].

$\text{CoFe}/\text{CoFe}_2\text{O}_4$  embedded in N-doped hollow carbon spheres ( $\text{CoFe}/\text{CoFe}_2\text{O}_4@\text{NC}$ ) with a high degree of oxygen vacancies was synthesized through pyrolysis, carbonization and partial reduction [84]. The catalyst exhibited high ORR activity (half-wave potential: 0.86 V) and a low overpotential of 0.36 V at  $10\text{ mA cm}^{-2}$  for the OER. The excellent performance was ascribed to the enhanced intrinsic activity of  $\text{CoFe}_2\text{O}_4$  spinel and improved electrical conductivity due to the strong coupling effect CoFe and  $\text{CoFe}_2\text{O}_4$ .

#### 2.4. Bi- and Multi-Metallic Catalysts

The design of bimetallic alloys with atomically precise noble metal loading attracts great interest in the field of ZABs. Unlike disordered perovskites, structurally ordered

intermetallic phases provide much better control over electronic effects, resulting in compositional and positional order and, therefore, more uniform active sites.

Bimetallic CoFe clusters were dispersed onto hollow carbon nanospheres (designated as FeCo-SA/CS) to produce a bifunctional catalyst with a cyclability of over 100 h at a current density of  $5 \text{ mA cm}^{-2}$  [85]. The catalyst showed an ORR onset potential of 0.96 V. For OER, the catalyst attained a current density of  $10 \text{ mA cm}^{-2}$  at an overpotential of 0.36 V. Mesoporous FeCo-N-C nanofibers with embedding FeCo nanoparticles were prepared from electrospun FeCo-N coordination compounds with bicomponent polymers consisting of polyvinylpyrrolidone (PVP) and polyacrylonitrile (PAN). The hybrid nanofibers exhibited 1D mesoporous structure with a large surface area and uniformly distributed active sites. The co-existence of FeCo nanoparticles and FeCo-N active sites promoted the catalytic activity of ORR and OER simultaneously [86].  $\text{Ni}_3\text{Fe-N}$  nanoparticles derived from ultrathin  $\text{Ni}_3\text{Fe-LDHs}$  were used by thermal ammonolysis and demonstrated a high OER activity [87]. The excellent performance of the  $\text{Ni}_3\text{Fe-N}$  catalyst derives from the intrinsic metallic character and unique electronic structure of this compound, which improves the electrical conductivity and adsorption of  $\text{H}_2\text{O}$ . In such intermetallic clusters, strong interaction between the two metals provides long-term stability and avoids deactivation.

Several Pt alloys with a transient metal possess superior ORR activities in which the origin of this higher activity is based on the modification of the electronic structure of Pt, which can affect the adsorption strength of oxygen-containing species on active sites. Here, a volcano relationship was demonstrated by Nørskov (Figure 6) [88]. For the best catalyst performance, the adsorption energy should be neither too small nor too big to balance reactant adsorption enthalpy and product desorption enthalpy. Similar relationships were established for PtM bimetallic catalysts with different metals and Pt/M molar ratios. For example, the TOF of the CuPt catalyst was increased by 60-fold over that of the Pt catalyst [89]. In addition, Pt-skin-like surfaces in bimetallic catalysts provide more active sites and higher ORR activities [90]. However, Pt alloyed with transition metals also tends to suffer from leaching and dissolution, which leads to insufficient stability and undermines the advantages of Pt alloy catalysts [91]. Therefore, core-shell bimetallic catalysts with Pt shell were developed to protect the transition metal core [92]. In these catalysts, the dissolution of core is mitigated and the interaction between Pt and the transition metal changes the electronic structure of Pt in a desirable direction. In addition, maximum Pt dispersion is achieved. In this way, a bifunctional  $\text{Fe}_3\text{Pt}$  nanoalloy supported onto  $\text{Ni}_3\text{FeN}$  was developed [93]. In this catalyst, the  $\text{Ni}_3\text{FeN}$  clusters considerably enhanced the activity of OER, whereas  $\text{Fe}_3\text{Pt}$  enhanced the activity of ORR as compared with commercial Pt/C and Ir/C catalysts at the same current density of  $10 \text{ mA cm}^{-2}$ .

Recent studies have indicated that the interaction between PtM catalysts and M-N-C supports demonstrates a synergistic effect to promote the ORR performance of these composite catalysts. For example, a highly active ternary PtZnCu catalyst within an N-doped carbon substrate was reported [94]. The catalyst was synthesized by pyrolysis of Pt, Zn and Cu precursors on the surface of the carbon support under a 5%  $\text{H}_2/\text{Ar}$  flow at  $750^\circ\text{C}$  for 2 h. The synthesis method proposed by the authors provides a straightforward way for large-scale synthesis of bifunctional electrocatalysts reducing catalyst costs and improving atom efficiency. The half-wave potential was 0.93 V for the ORR in an acidic solution.

A magnetic field strategy was introduced in obtaining graphene-supported bimetallic Pt-Ni catalysts with predominant (111) facets as efficient ORR catalysts. In this way, a set of porous PtNi catalysts on graphene (G) with Pt/Ni molar ratios of 0.1, 0.5, 0.6, 1.8 and 2.4 was developed by Lyu et al. under high magnetic field in the range of 0.5–2 T [95]. The interaction between the nanoparticles produces microscopic Lorentz forces and improves interaction between Pt and Ni precursors, thus controlling the composition. The  $\text{Pt}_{2.4}\text{Ni/G}$  catalyst synthesized under 2 T showed a 5.1 times higher ORR rate than that of a commercial Pt/C catalyst.

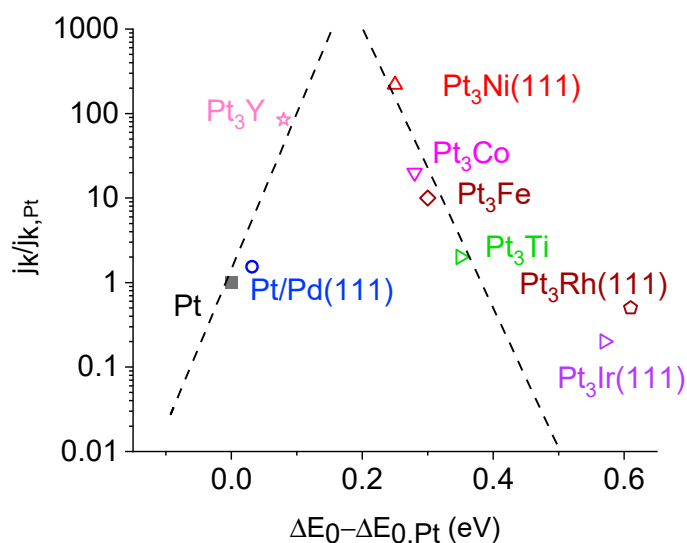


**Figure 6.** Volcano plot of ORR kinetic current density ( $j_k$ ) as a function of calculated oxygen adsorption energy ( $\Delta E_0$ ) for Pt alloy electrocatalysts in acidic electrolytes. The dashed lines are the theoretical predictions from [96].

Ordered intermetallic compounds such as  $\text{PdZn}_3$  were reported to possess excellent catalytic selectivity and stability for the selective semihydrogenation of acetylene alcohols [97]. However, so far, the studies on bimetallic PdM catalysts for ZABs remain very limited. This is mainly due to the lack of effective synthetic methods to control particle sizes during the high temperature annealing [98]. This requires answering two important questions: what annealing temperature is suitable for the formation of structurally ordered phases, and what factors control the ordering kinetics. Therefore, these factors should be studied and then a suitable synthetic route can be adopted. A successful synthesis of ordered  $\text{Pd}_3\text{Pb}$  intermetallic phase with small particle size was reported [99]. Potassium triethylborohydride ( $\text{KEt}_3\text{BH}$ ) or lithium triethylborohydride ( $\text{LiEt}_3\text{BH}$ ) were used as reducing agents in THF because they both have fast reduction kinetics and can provide the coreduction of Pd and Pb precursors. The obtained sample was annealed for 12 h. The rate of formation of the intermetallic phase was dominated by solid-state diffusion that increases exponentially with annealing temperature. Above  $400^\circ\text{C}$ , there were superlattice peaks in XRD spectra (so-called “ordering peaks”), indicating that the intermetallic phases were formed. It was reported that a high annealing temperature promotes the formation of the ordered phase, but also leads to particle size growth of  $\text{Pd}_3\text{Pb}$  nanoparticles. For the samples annealed at 600 and  $800^\circ\text{C}$ , the particle size increased from 4 nm to 7 and 12 nm, respectively. Therefore, a lower temperature of  $400^\circ\text{C}$  was chosen to prepare the bimetallic  $\text{Pd}_3\text{Pb}/\text{C}$  catalyst. This catalyst demonstrated a significant enhancement in catalytic activity and durability for the ORR when compared with a Pd/C commercial catalyst.

Ag-based bimetallic formulations were found to have adequate ORR activity. The high reactivity for ORR over the  $\text{PdAg}_9$  bimetallic catalysts was reported by the Stevenson group [100]. These authors produced bimetallic nanoalloys via coreduction of Ag and Pd carboxylic acid complex precursors in the presence of stabilizing ligands. In these catalysts, the Pd atoms facilitate the binding of the oxygen and subsequently the Ag atoms facilitate the desorption of the reaction products such as OH. The 9:1 Ag:Pd molar ratio exhibits a suitable geometric arrangement allowing to work by an ensemble effect. The full four-electron process takes place by combining the fast kinetics of Pd for the adsorption with rapid disproportionation on Ag for the desorption step. The data suggest a correlation between the bimetallic interaction developed at the nanoscale and the observed high catalytic activity.

Cu is a suitable sacrificial agent to be galvanically displaced by Pd for preparation of bimetallic alloys. In this way, Lüsi et al. showed the use of galvanic displacement on a Cu film to prepare PdCu catalysts for the ORR reaction in alkaline media [101]. A two-step method was employed by Betancourt et al. to obtain an active bimetallic catalyst. First, they reduced a Cu precursor onto a commercial Ag/C catalyst to form AgCu/C nanoparticles and then performed galvanic displacement of Cu to deposit an atomically dispersed loading of Pd [102]. The PdAg/C catalyst outperformed conventional Pd/C and Ag/C commercial catalysts in the ORR reaction. The synergistic effect of Pd and Ag plays a key role in electrode reactions. A similar method for preparation of a supported AuCu bimetallic catalyst for the air electrode was recently patented [103]. The method did not require the addition of a surfactant, is suitable for large-scale production, and the catalyst has large open porosity which provided a high diffusion rate to the catalytic sites.

### 2.5. Layered Double Hydroxides

The layered double hydroxides (LDH),  $[M^{2+}_{1-x}M^{3+}_x(OH)_2][A^{n-}]_{x/n} \cdot zH_2O$ , have unique structural properties due to incorporated anions and water between the large interlayer spaces. They belong to multi-metal clay materials which consist of charged balancing anions,  $A^{n-}$ , intercalated within brucite-like sheets of divalent,  $M^{2+}$ , and trivalent,  $M^{3+}$ , metal cations [104]. LDHs are able to combine electrochemically active elements such as Co, Ni, Fe, and many others. NiFe-LDH nanostructures are regarded as the most promising of OER catalysts due to their special electronic configuration as discussed in previous sections. The composition of LDHs can be easily tuned, resulting in the unique redox characteristics and notable catalytic activity during the OER [105]. Ni–O and Fe–O bond distances are comparable, thus, these two metals can replace each other and form edge-sharing  $FeO_6$  and  $NiO_6$  octahedra. Due to their semiconductor characteristics, a Schottky barrier may be formed when contacting the conductive substrate, which greatly hinders the charge transfer. Therefore, various strategies including size modulation, heteroatom doping, and surface and defect engineering were developed to improve the electrocatalytic performance of LDHs towards OER [106].

The physical and chemical properties of LDHs vary greatly when the dimensions of nanostructures are down to 1-nm scale, thus, the controllable and convenient fabrication of ultrathin nanocrystals is highly desirable for potential applications in ZABs. The exfoliation of LDH structure into a few layers and single sheets can expose more surface sites because of the large interlayer spacing between individual layers in the LDH structure. However, developing an effective strategy to exfoliate bulk NiFe-LDHs into stable single-layer nanosheets with more exposed active sites remains challenging. The synthesis requires a complex multistep process (i.e., hydrothermal process, anion exchange, and exfoliation) which takes several days to obtain the final product. Additionally, the refined morphology of as-synthesized LDH nanosheets obtained by exfoliation cannot be controlled precisely, as the high charge density of LDHs makes it harder to be exfoliated into monolayers.

In the bottom-up synthesis method, a surfactant (e.g., sodium dodecyl sulfonate) is introduced to form micelles in which LDH nanostructures are grown in a confined space. Recently two dimensional NiFe-LDHs nanosheets (1.3 nm) were obtained with a synthesis time of only 5 min [107]. They demonstrated enhanced OER performance compared with bulk NiFe-LDHs catalysts obtained via the coprecipitation method. In the bottom-up method modulating the crystallinity to fabricate a partially amorphous structure is a promising strategy in enhancing the electro-oxidation performances, which could achieve an optimal balance between active sites and conductivity. NiFe-LDH nanosheet arrays were in-situ grown on a NiFe alloy foam, which formed a self-supported anode with partially amorphous nanosheets providing reactive sites for the electrochemical generation of high-valence species. This also resulted in rich crystalline–amorphous interfaces to form and stabilize  $Ni^{3+}$  ions. Furthermore, the highly porous and conductive framework around the nanosheets further improved the electrocatalytic rate [108].

The higher intrinsic OER performance of NiFe-LDHs is further confirmed by other studies of NiFe-LDHs grown on different carbon materials (carbon quantum dots, graphitized carbon, 3D macro/mesoporous carbon, and graphene). A facile strategy to create ultrathin NiFe-LDHs nanosheets grown on carbon nanotubes (CNTs) was proposed [109]. Unlike bulk NiFe-LDH nanomaterials, the CNTs-supported catalysts demonstrated different 1D/3D layered structures, and electron transfer properties, thereby improving the OER performance.

The nature of active sites of NiFe-LDHs remain unclear, and thus, further mechanistic studies are helpful to understand the structure–activity correlation. Currently trial-and-error iterative design of bifunctional catalysts remains the main approach in this area. However, a more systematic approach is needed to achieve a major breakthrough. To this end, MOFs and single atom engineering are promising research directions that could pave the way for the systematic optimization of catalysts. Therefore, future studies should expand the limited understanding of the precise formation mechanisms behind MOFs to enable a more methodical tuning of catalyst materials. Upcoming research efforts should also focus on the stabilization of high-loading SACs, which is the main obstacle hindering their practical applications.

Other LDHs, such as CoMn, NiMn, and CoNi are still in the early stages of development of a bifunctional catalysts. They are typically anchored to porous conductive supports, such as N-doped graphene or carbon [110,111]. Such materials have large surface area and unique porous structure. Although the simple deposition method does not fully protect from corrosion in the alkaline electrolyte, excellent OER activity of NiMn LDH and NiCo<sub>2</sub>O<sub>4</sub>@NiMn composites was reported. It can be concluded that layered double hydroxides is one of the most effective OER catalysts due to their excellent activity and high stability in alkaline conditions.

### 3. Effect of an External Magnetic Field

Recent studies have shown that applying an external magnetic field is a simple and effective strategy to improve the electrocatalytic performance of non-precious metal catalysts. Electrocatalysis enhanced by the alternating magnetic field (AMF) may include the spin-polarization effect, magnetothermal effect, magnetohydrodynamic effect, and Néel relaxation. For example, magnetohydrodynamic effect occurs when a magnetic field interacts with charged ions, causing a macroscopic and microscopic convection which can change mass transfer rates of active species, reduce polarization resistance, and decrease bubble resistance caused by ohmic drop. The oxygen bubble escape rate increases significantly under AMF. The magnetothermal effect can increase the local temperature of magnetic catalysts resulting in enhancing the kinetics of OER [112]. In addition, composite magnetic catalysts can generate heat locally under AC magnetic field due to the internal flip of spins relative to the crystalline lattice (Néel relaxation) thereby increasing catalyst temperature [113–116]. Recent studies have revealed that structurally stable catalysts can undergo spin-state flipping changes by applying magneto-thermal perturbations using AMF, without altering their structure. Strain may also be the mechanism of magnetic field enhancement. Liu et al. [117] explored the change of the electrocatalytic performance of an FeCo catalyst in the OER under a magnetic field and proposed that strain would occur in the FeCo alloy, reducing OER overpotential. In general, magnetic field-enhanced electrocatalysis has multiple mechanisms acting together. In many cases, the stronger the magnetic properties of catalysts, the more significant the promoting effect is. However, most electrocatalysts undergo surface reconstruction in the alkaline OER process, and paramagnetic oxyhydroxide species can be formed on their surface reducing the magnitude of this effect.

#### 3.1. Spin Polarization Effect

Research on magnetic spin-selective catalytic reactions and spin polarization dynamics is limited for OER in alkaline solutions. To quantify this effect, the exploration of promoting

parallel spins to improve the OER activity was extensively studied. The formation of O–O bonds in the production of O<sub>2</sub> requires spin conservation of the paramagnetic triplet, making the catalyst's activity on the oxygen surface during spin polarization critical for achieving a parallel spin arrangement. The alternating magnetic field (AMF) was reported to reduce the energy barrier in transition metal oxide catalysts required for electron transition during the OER process [118]. Many transition metal oxide catalysts show that the magnetic susceptibility and AMF field enhances the spin energy states of electrons [119]. The formation of paramagnetic triplet oxygen molecules ( $\uparrow\text{O}=\text{O}\uparrow$ ) during the OER is related to the spin of electrocatalysts [120–122].

Current research on the mechanism of electron spin interaction mainly involves catalysts with ferromagnetic properties. Ferromagnetic catalysts have an ordered magnetic moment structure and spin polarization, which makes them a good model system in understanding how spin polarization affects the OER mechanism and kinetics under AMF. For example, the OER overpotential over a Co<sub>0.4</sub>Ni<sub>0.6</sub>-MOF-74 catalyst reduced by 36% under a 150 kHz, 5.5 mT AMF at a current density of 10 mA cm<sup>-2</sup>, as compared with that without magnetic field [123]. The promoting effect on OER often has a maximum at a specific intensity of AMF. For example, a maximum was observed at a magnetic field of 4.3 mT over ZIF-67-supported cobalt-based electrocatalysts with different magnetic properties (Co, CoO and Co<sub>3</sub>O<sub>4</sub>) (Figure 7a). At optimal conditions, the overpotential over ZIF-67-supported Co, CoO and Co<sub>3</sub>O<sub>4</sub> catalysts was reduced by 140, 119, and 142 mV, respectively, relative to those in experiments without AMF. Further increase in the magnetic field intensity increased the overpotential due to electromagnetic induction [122]. The Co catalyst demonstrated the largest current density of 15.6 mA cm<sup>-2</sup> (Figure 7b). Due to the thermal insulation of individual Co clusters, magnetic heating was strictly confined to magnetic ions. In the course of reaction, the adsorbed hydroxyl groups deprotonated on the surface to form O radicals, where a Co d<sub>π</sub>-orbital electron and an p<sub>π</sub>-orbital electron of oxygen showed the same spin configuration due to exchange interaction effects (Figure 7c) [124]. In the subsequent process of adsorption of OH-groups and deprotonation, electrons with specific spin directions were selectively removed through ferromagnetic exchange effects, thereby promoting the generation of triplet oxygen (Figure 7d) [125]. The formation of paramagnetic triplet oxygen occurs by similar mechanisms under DC and AC magnetic field. This can effectively reduce overpotential and increase the rate of electrochemical reaction. A similar behavior was reported over a NiFe<sub>2</sub>O<sub>4</sub>@MOF-74 catalyst. The overpotential in hydrogen evolution reaction was reduced by 30 mV at 10 mA cm<sup>-2</sup> under an AMF of 2.3 mT [126]. It should be mentioned that this effect was not observed with CoO and other magnetic catalysts with weak exchange interaction.

A similar promoting effect was observed over core-shell NiFe<sub>2</sub>O<sub>4</sub>@(Ni, Fe)S/P catalysts when the overpotential in OER reduced from 323 to 176 mV at a 4.3 mT [127]. The authors noted hindering of the ion diffusion under AMF which could indicate that there is an optimum magnetic field at which the reaction rate has a maximum value. The OER process is a mass transfer limited reaction under higher reaction rates and, therefore, is influenced by the slow diffusion of reactants under AMF. In a catalytic reactor in which both electric and magnetic fields are present, moving ions are affected by the Lorentz forces of the electric and magnetic fields and change their original path, resulting in a slower mass transfer rate.

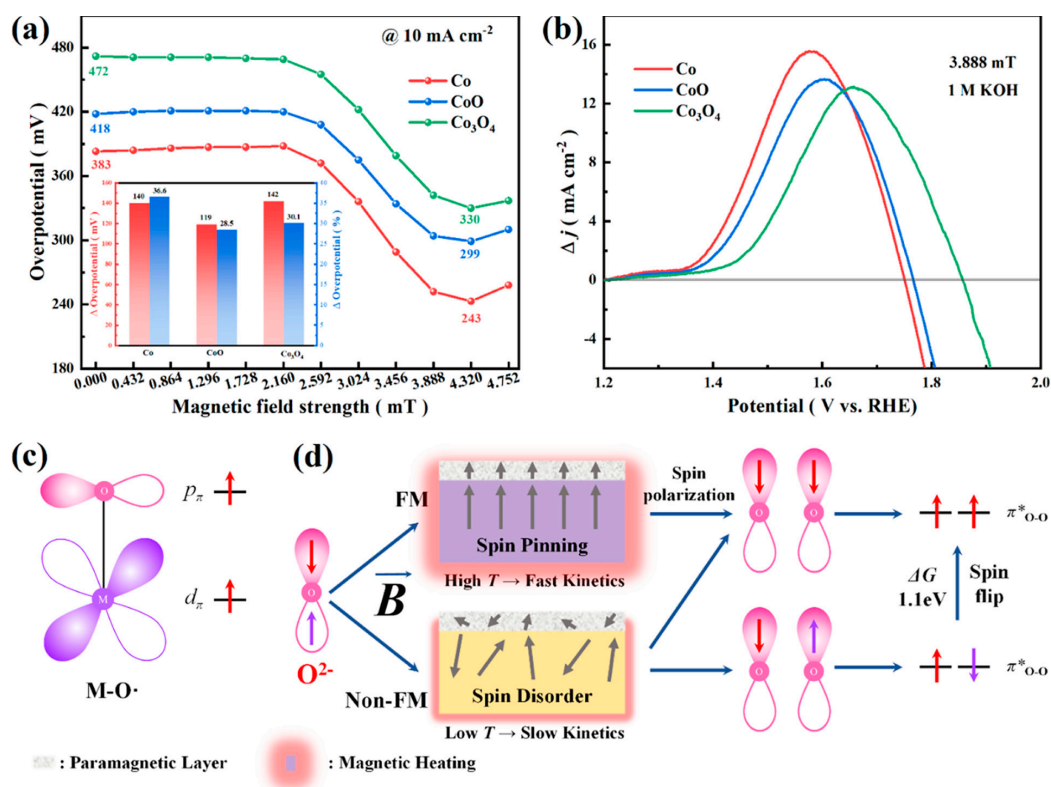


**Figure 7.** (a) Overpotential at a current density of  $10 \text{ mA cm}^{-2}$  under different AMF. (b) Maximum current density of Co, CoO, and Co<sub>3</sub>O<sub>4</sub>. (c) Spin configuration of M–O. (d) Schematic of the difference in the OER promotion mechanism of different magnetic electrocatalysts under AMF. Reprinted with permission from [122]. Copyright 2022, American Chemical Society.

As was discussed in Section 2.5, Ni, Co, and Fe metal layered double hydroxides (LDHs) are commonly used as catalysts for the OER in alkaline electrolytes. The iron group transition metals, including Fe<sup>3+</sup> ( $t_{2g}^3 e_g^2$ ), Co<sup>2+</sup> ( $t_{2g}^6 e_g^1$ ), and Ni<sup>2+</sup> ( $t_{2g}^6 e_g^2$ ), have a spin single electron, therefore, these catalysts are often seen as a model system for studying the spin-magnetic effect. The effective bonding p-orbitals of oxygen intermediates are crucial to enhancing OER reaction. Based on symmetry conservation and LDH planar structures, orbitals perpendicular to the plane orientation (out-of-plane orbitals including  $d_{z^2}$ ,  $d_{xz}$ , and  $d_{yz}$ ) favor reactant adsorption, while orbitals parallel to the LDH planes (in-plane orbitals including  $d_{x^2-y^2}$  and  $d_{xy}$ ) favor electron transport [128]. The introduction of an external magnetic field enhances the spin-electron exchange between LDH catalysts and oxygen-containing intermediates, thereby enhancing the OER rate.

In addition to direct application of ferromagnetic catalysts, doping specific ions into LDH is another strategy to create active OER catalysts. Sun et al. used this strategy to introduce Cu<sup>2+</sup> ions into NiFe-LDH catalyst. The Cu<sup>2+</sup> orbital can induce spin splitting at Fe(III) sites and excite electrons near the Fermi level, which facilitates adsorption of O<sup>-</sup> containing species [129]. The Cu<sub>1</sub>Ni<sub>6</sub>Fe<sub>2</sub>-LDHs demonstrated a low overpotential of 210 mV at  $10 \text{ mA cm}^{-2}$ , which is one of the best OER activities reported. In general, the composite structure formed from two different magnetic materials can lead to magnetic inversion, thus triggering the catalytic activity. This strategy provides a new approach for catalyst design: doping magnetic materials to non-magnetic electrocatalysts and using magnetic field to enhance their performance [130]. Alternatively, composites of non-magnetic and magnetic catalysts can be designed using rational structural design by changing the electron configuration and breaking the symmetry, making the whole catalyst magnetic and, therefore, triggered by magnetic field.

### 3.2. Magnetothermal Effect

The spin polarization inversion of ferromagnetic materials under alternating magnetic fields induces a local magnetic heating effect to improve charge transfer efficiency, and the heated active site accelerates the adsorption/desorption process, resulting in faster catalytic reaction kinetics. This effect of local catalyst heating under AMF seems to be more important as compared with the spin-polarization effect. Gong et al. [131] showed that a Co@MoS<sub>2</sub> SAC demonstrated the appearance of in-plane ferromagnetic properties, that facilitated the parallel spin arrangement of oxygen atoms under 300 kHz, 4.55 mT AMF. As a result, the overpotential in OER reduced from 317 to 250 mV at a current density of 10 mA cm<sup>-2</sup>, compared with when AMF was not applied. AMF is a promising methodology for further improving magnetic single-atom catalyst (SAC) activity. This approach is also applicable to other magnetic SACs, which provides a new avenue for improving the OER activity by application of a weak AMF.

A ferromagnetic Co/ZIF-67 catalyst showed the highest specific heating rate among ZIF-67-supported Co, CoO and Co<sub>3</sub>O<sub>4</sub> catalysts and, therefore, the Co/ZIF-67 catalyst demonstrated the best performance in OER under AMF [122]. Magneto-thermal effect enhanced the catalytic performance of nickel-coated iron carbide nanoparticles (FeC–Ni) in the OER under AMF [132]. Local heating of the catalyst reduced the overpotential required for oxygen release in an alkaline electrolyte by 0.2 V. Using the same approach, Peng et al. developed a superparamagnetic NiFe@NiFeOOH core–shell catalyst [133]. The OER overpotential reduced to 209 mV at 10 mA cm<sup>-2</sup> over this catalyst under AMF. The catalyst possesses a remarkable catalytic stability: no detachment of FeOOH or NiOOH was observed during the long-term operation.

Magnetic Cr<sub>2</sub>Ge<sub>2</sub>Te<sub>6</sub> nanosheet catalyst was demonstrated to improve the OER performance by the application of an external magnetic field [134]. The improvement was a combined effect of the Lorentz force generated by magnetic field and local magnetic heating. Furthermore, Cr<sub>2</sub>Ge<sub>2</sub>Te<sub>6</sub> with fewer layers has intrinsic spin and charge density dual bipolar tunable properties, which makes it a potential application in the field of spin electrocatalysis. Yuan synthesized 3D screw pyramid MoS<sub>2</sub> catalyst with abundant edge active sites [135]. Eddy current inside the nanosheets contributed to magnetic heating and the rate of HER over the screw pyramid MoS<sub>2</sub> catalysts are greatly improved compared with step pyramid MoS<sub>2</sub> under AMF. This example provides a promising guideline for eddy current assisted electrocatalytic enhancement of multilayered transition metal disulfides.

## 4. Conclusions and Outlook

Several categories of catalytic materials ranging from monometallic noble metal catalysts to alternative carbons, mixed metal oxides, spinels, perovskites and inorganic–organic composites have been discussed as catalysts for OER/ORR reactions as well as susceptor materials under alternating magnetic field with demonstrated influential factors to their performance and/or catalytic properties. Some basic synthetic strategies have also been presented. A few fundamental aspects including the OER/ORR reaction mechanisms over novel catalysts, should be studied to guide the design of high-efficiency air electrode catalysts. The large overpotential and slow kinetics at the cathode appear to be the major challenges that limit the practical electrochemical performances.

The single metal catalysts exhibit better ORR catalytic activity than the nanoparticles. The Pt-based noble metal family generally possesses virtues of both high activity and favorable stability but disadvantages of high cost. Making bimetallic catalysts with cheap transition metals and using Pt as a shell in core–shell catalysts are effective routes to lower the noble metal loading and further enhance the stability of the transition metals. Carbon-based materials, transition-metal oxides, and composite catalysts derived from polymers are promising abundant and cheap catalysts applicable for OER/ORR reactions. In particular, graphene and N-doped carbon nanotubes are attractive candidates for future research due to their high activity, high electrical conductivity and chemical stability. Layered double hydroxides (LDHs) are considered as cost-effective OER catalysts due to their excellent

activity and stability in an OER in alkaline electrolytes. Their synthesis does not require lengthy, complicated steps, which opens good perspectives for scale-up. The combination of nitrogen-doped carbon materials with SAC or metal nanoparticles produces very active and stable bifunctional catalysts.

Proposed future research directions in these non-precious metal catalytic materials include: (i) exploiting the effect of physiochemical parameters (composition, morphology, oxidation state, defects, surface area, conductivity, etc.) on the intrinsic catalytic activity, (ii) increasing the density of active sites and their utilization through innovative design of materials and structures including single atom stabilization, and (iii) optimizing catalyst synthesis strategies (cheaper precursors, low temperature, shorter duration) to scale up their synthesis to industrial scale without decreasing their activity and stability.

The dissolution and irreversible oxidation of active metals are among the main reasons for ZAB failure and large overpotential in the charge–discharge process.

The application of an external magnetic field is an elegant strategy to enhance electrocatalytic rates and to reduce the overpotential. Studies performed help to understand the effect of the external magnetic field on the performance of ferromagnetic composite electrocatalysts employed in ZABs. Many studies were performed under a DC magnetic field, and there is still a lack of systematic understanding of the role of AC magnetic field in OER electrocatalysis. The capacity of inductive heating to drive heat directly to the catalytic sites turned out to be an enabling technology capable of increasing the rate of OER by an order of magnitude under AC magnetic field. The removal of mass transfer limitation over the reactor wall has reduced the concentration gradients in ZABs, largely contributing to the improvement of energy efficiency as well as the reduction in overpotential. Several studies showed that the magnetic field enhances the catalytic performance in a volcanic pattern, where high magnetic field intensity inhibits the reaction rate. This effect was explained as a counterplay between spin polarization and magnetohydrodynamic effect.

Although there have been several studies on the electron spin selectivity mechanism, related to changes in the electron spin structure of the catalyst, there is a need for in situ characterization of spintronic structures to better understand the theory and mechanism of spin catalysis.

**Funding:** This research was funded by the European Research Council Synergy Grant SCOPE No. 810182.

**Data Availability Statement:** The authors confirm that the data supporting the findings of this study are available within the article.

**Conflicts of Interest:** The authors declare no conflict of interest.

## References

1. Cole, W.; Frew, B.; Gagnon, P.; Reimers, A.; Zuboy, J.; Margolis, R. Envisioning a low-cost solar future: Exploring the potential impact of achieving the SunShot 2030 targets for photovoltaics. *Energy* **2018**, *155*, 690–704. [CrossRef]
2. Bellini, E. Portuguese Government Confirms World Record Solar Price of \$0.01316/kWh. *PV Mag. Int.* **2020**. Available online: <https://www.pv-magazine.com/2020/08/27/portuguese-government-confirms-world-record-solar-price-of-0-01316-kwh> (accessed on 24 July 2023).
3. He, W.; King, M.; Luo, X.; Dooner, M.; Li, D.; Wang, J. Technologies and economics of electric energy storages in power systems: Review and perspective. *Adv. Appl. Energy* **2021**, *4*, 100060. [CrossRef]
4. International Energy Agency Global EV Outlook 2020: Entering the Decade of Electric Drive? *IEA Paris* **2020**. Available online: <https://www.iea.org/reports/global-ev-outlook-2020> (accessed on 24 July 2023).
5. Zeng, X.; Li, M.; Abd El-Hady, D.; Alshitari, W.; Al-Bogami, A.S.; Lu, J.; Amine, K. Commercialization of lithium battery technologies for electric vehicles. *Adv. Energy Mater.* **2019**, *9*, 1900161. [CrossRef]
6. Han, X.; Li, X.; White, J.; Zhong, C.; Deng, Y.; Hu, W.; Ma, T. Metal–air batteries: From static to flow system. *Adv. Energy Mater.* **2018**, *8*, 1801396. [CrossRef]
7. Shaulova, E.; Biagi, L. Lithium Industry Worldwide. Statistics Report on the Global Lithium Industry. 2023. Available online: <https://www.statista.com/study/40094/lithium-statista-dossier> (accessed on 24 July 2023).
8. Ellis, D. Lithium-Ion Batteries Demand to Grow 30% a Year—McKinsey. *Mining* **2022**. Available online: <https://miningdigital.com/supply-chain-and-operations/lithium> (accessed on 24 July 2023).

9. FCAB. Executive Summary. National Blueprint for Lithium Batteries 2021–2030. 2021. Available online: <https://www.energy.gov> (accessed on 24 July 2023).
10. BMI. BYD Becomes Benchmark's 7th Tier One EV Battery Manufacturer; 2nd China Cell Maker. 2021. Available online: <https://www.benchmarkminerals.com/membership/byd-becomes-benchmarks-7th-tier-one-ev-battery-manufacturer-2nd-china-cell-maker-2/> (accessed on 19 May 2023).
11. Leong, K.W.; Wang, Y.; Ni, M.; Pan, W.; Luo, S.; Leung, D.Y.C. Rechargeable Zn–air batteries: Recent trends and future perspectives. *Renew. Sustain. Energy Rev.* **2022**, *154*, 111771. [[CrossRef](#)]
12. Khan, P.A.; Venkatesh, B. *Economic Analysis of Chemical Energy Storage Technologies*; Springer: Berlin/Heidelberg, Germany, 2016; pp. 277–291.
13. O'Neill, A. *World Bank Commodities Price Forecast*; World Bank: Washington, DC, USA, 2022.
14. Fu, J.; Liang, R.; Liu, G.; Yu, A.; Bai, Z.; Yang, L.; Chen, Z. Recent progress in electrically rechargeable zinc–air batteries. *Adv. Mater.* **2019**, *31*, 1805230. [[CrossRef](#)]
15. Kiss, A.M.; Myles, T.D.; Grew, K.N.; Peracchio, A.A.; Nelson, G.J.; Chiu, W.K.S. Carbonate and bicarbonate ion transport in alkaline anion exchange membranes. *J. Electrochem. Soc.* **2013**, *160*, F994–F999. [[CrossRef](#)]
16. Zhang, W.; Liu, Y.; Zhang, L.; Chen, J. Recent advances in isolated single-atom catalysts for zinc air batteries: A focus review. *Nanomaterials* **2019**, *9*, 1402. [[CrossRef](#)]
17. Hu, C.; Lin, Y.; Connell, J.W.; Cheng, H.; Gogotsi, Y.; Titirici, M.; Dai, L. Carbon-based metal-free catalysts for energy storage and Environmental Remediation. *Adv. Mater.* **2019**, *31*, 1806128. [[CrossRef](#)] [[PubMed](#)]
18. Meffre, A.; Mehdaoui, B.; Kelsen, V.; Fazzini, P.F.; Carrey, J.; Lachaize, S.; Respaud, M.; Chaudret, B. A Simple Chemical Route toward Monodisperse Iron Carbide Nanoparticles Displaying Tunable Magnetic and Unprecedented Hyperthermia Properties. *Nano Lett.* **2012**, *12*, 4722–4728. [[CrossRef](#)] [[PubMed](#)]
19. Li, B.; Ge, X.; Goh, F.W.T.; Hor, T.S.A.; Geng, D.; Du, G.; Liu, Z.; Zhang, J.; Liu, X.; Zong, Y. Co<sub>3</sub>O<sub>4</sub> nanoparticles decorated carbon nanofiber mat as binder-free air-cathode for high performance rechargeable zinc-air batteries. *Nanoscale* **2015**, *7*, 1830–1838. [[CrossRef](#)] [[PubMed](#)]
20. Yuxin, Z.; Ying, Y.; Chunzhen, Z.; Meipeng, Z.; Yue, W.; Fengliang, Z.; Lili, R. Air cathode catalyst layer ink suitable for aerosol printing and preparation method thereof. Patent CN113871761A, 31 December 2021.
21. Pi, Y.-T.; Xing, X.-Y.; Lu, L.-M.; He, Z.-B.; Ren, T.-Z. Hierarchical porous activated carbon in OER with high efficiency. *RSC Adv.* **2016**, *6*, 102422–102427. [[CrossRef](#)]
22. Tang, J.; Liu, J.; Li, C.; Li, Y.; Tade, M.O.; Dai, S.; Yamauchi, Y. Synthesis of Nitrogen-doped mesoporous carbon spheres with extra-large pores through assembly of diblock copolymer micelles. *Angew. Chem. Int. Ed.* **2014**, *54*, 588–593. [[CrossRef](#)]
23. Fukuyama, H.; Terai, S. Preparing and characterizing the active carbon produced by steam and carbon dioxide as a heavy oil hydrocracking catalyst support. *Catal. Today* **2008**, *130*, 382–388. [[CrossRef](#)]
24. Zhang, X.; Yan, P.; Zhang, R.; Liu, K.; Liu, Y.; Liu, T.; Wang, X. A novel approach of binary doping sulfur and nitrogen into graphene layers for enhancing electrochemical performances of supercapacitors. *J. Mater. Chem. A* **2016**, *4*, 19053–19059. [[CrossRef](#)]
25. Sun, L.; Zhou, H.; Li, L.; Yao, Y.; Qu, H.; Zhang, C.; Liu, S.; Zhou, Y. Double soft-template synthesis of nitrogen/sulfur-codoped hierarchically porous carbon materials derived from protic ionic liquid for supercapacitor. *ACS Appl. Mater. Interfaces* **2017**, *9*, 26088–26095. [[CrossRef](#)]
26. Gupta, S.; Zhao, S.; Xu, H.; Wu, G. Highly stable nanocarbon catalysts for bifunctional oxygen reduction and evolution reactions in alkaline media. *ECS Meet. Abstr.* **2017**, MA2017-01, 1423. [[CrossRef](#)]
27. McCrory, C.C.L.; Jung, S.; Peters, J.C.; Jaramillo, T.F. Benchmarking Heterogeneous electrocatalysts for the oxygen evolution reaction. *J. Am. Chem. Soc.* **2013**, *135*, 16977–16987. [[CrossRef](#)]
28. Lee, D.U.; Park, H.W.; Higgins, D.; Nazar, L.; Chen, Z. Highly active graphene nanosheets prepared via extremely rapid heating as efficient zinc-air battery electrode material. *J. Electrochem. Soc.* **2013**, *160*, F910–F915. [[CrossRef](#)]
29. Chengen, G.H.; Chao, G.X. Carbon-coated graphene/metal oxide composite material and preparation method thereof. Patent CN113690429A, 23 August 2021.
30. Zhou, Q.; Zhang, Z.; Cai, J.; Liu, B.; Zhang, Y.; Gong, X.; Sui, X.; Yu, A.; Zhao, L.; Wang, Z.; et al. Template-guided synthesis of Co nanoparticles embedded in hollow nitrogen doped carbon tubes as a highly efficient catalyst for rechargeable Zn–air batteries. *Nano Energy* **2020**, *71*, 104592. [[CrossRef](#)]
31. Long, J.; Chen, C. Fe-based bimetallic zinc-air battery cathode catalyst based on layered MOF. Patent CN113097513A, 2 April 2021.
32. Jaksic, J.M.; Nan, F.; Papakonstantinou, G.D.; Botton, G.A.; Jaksic, M.M. Theory, substantiation, and properties of novel reversible electrocatalysts for oxygen electrode reactions. *J. Phys. Chem. C* **2015**, *119*, 11267–11285. [[CrossRef](#)]
33. Pan, J.; Xu, Y.Y.; Yang, H.; Dong, Z.; Liu, H.; Xia, B.Y. Advanced architectures and relatives of air electrodes in Zn–Air batteries. *Adv. Sci.* **2018**, *5*, 1700691. [[CrossRef](#)] [[PubMed](#)]
34. Li, Y.; Li, Q.; Wang, H.; Zhang, L.; Wilkinson, D.P.; Zhang, J. Recent Progresses in oxygen reduction reaction electrocatalysts for electrochemical energy applications. *Electrochem. Energy Rev.* **2019**, *2*, 518–538. [[CrossRef](#)]
35. Cheng, F.; Chen, J. Metal–air batteries: From oxygen reduction electrochemistry to cathode catalysts. *Chem. Soc. Rev.* **2012**, *41*, 2172. [[CrossRef](#)]

36. Sequeira, C.A.C. Carbon Anode in Carbon History. *Molecules* **2020**, *25*, 4996. [[CrossRef](#)] [[PubMed](#)]
37. Zamani-Meymian, M.-R.; Khanmohammadi Chenab, K.; Pourzolfaghar, H. Designing high-quality electrocatalysts based on CoO:MnO<sub>2</sub>@C supported on carbon cloth fibers as bifunctional air cathodes for application in rechargeable Zn–Air battery. *ACS Appl. Mater. Interfaces* **2022**, *14*, 55594–55607. [[CrossRef](#)]
38. Song, Z.; Han, X.; Deng, Y.; Zhao, N.; Hu, W.; Zhong, C. Clarifying the Controversial Catalytic Performance of Co(OH)<sub>2</sub> and Co<sub>3</sub>O<sub>4</sub> for oxygen reduction/evolution reactions toward efficient Zn–air batteries. *ACS Appl. Mater. Interfaces* **2017**, *9*, 22694–22703. [[CrossRef](#)] [[PubMed](#)]
39. Wu, Y.; Wu, X.; Tu, T.; Zhang, P.; Li, J.; Zhou, Y.; Huang, L.; Sun, S. Controlled synthesis of FeN<sub>x</sub>–CoN<sub>x</sub> dual active sites interfaced with metallic Co nanoparticles as bifunctional oxygen electrocatalysts for rechargeable Zn–air batteries. *Appl. Catal. B Environ.* **2020**, *278*, 119259. [[CrossRef](#)]
40. Xu, Y.; Deng, P.; Chen, G.; Chen, J.; Yan, Y.; Qi, K.; Liu, H.; Xia, B.Y. 2D Nitrogen-doped carbon nanotubes/Graphene hybrid as bifunctional oxygen electrocatalyst for long-life rechargeable Zn–Air batteries. *Adv. Funct. Mater.* **2020**, *30*, 1906081. [[CrossRef](#)]
41. Sun, X.; Gong, Q.; Liang, Y.; Wu, M.; Xu, N.; Gong, P.; Sun, S.; Qiao, J. Exploiting a high-performance “double-carbon” structure Co<sub>9</sub>S<sub>8</sub>/GN bifunctional catalysts for rechargeable Zn–Air batteries. *ACS Appl. Mater. Interfaces* **2020**, *12*, 38202–38210. [[CrossRef](#)]
42. Wang, Y.; Wu, M.; Li, J.; Huang, H.; Qiao, J. In situ growth of CoP nanoparticles anchored on (N,P) co-doped porous carbon engineered by MOFs as advanced bifunctional oxygen catalyst for rechargeable Zn–air battery. *J. Mater. Chem. A* **2020**, *8*, 19043–19049. [[CrossRef](#)]
43. Wu, Z.; Wu, H.; Niu, T.; Wang, S.; Fu, G.; Jin, W.; Ma, T. Sulfurated Metal–Organic framework-derived nanocomposites for efficient bifunctional oxygen electrocatalysis and rechargeable Zn–air battery. *ACS Sustain. Chem. Eng.* **2020**, *8*, 9226–9234. [[CrossRef](#)]
44. Guo, X.; Zheng, S.; Luo, Y.; Pang, H. Synthesis of confining cobalt nanoparticles within SiO<sub>x</sub> /nitrogen-doped carbon framework derived from sustainable bamboo leaves as oxygen electrocatalysts for rechargeable Zn–air batteries. *Chem. Eng. J.* **2020**, *401*, 126005. [[CrossRef](#)]
45. Zhang, H.-M.; Hu, C.; Ji, M.; Wang, M.; Yu, J.; Liu, H.; Zhu, C.; Xu, J. Co/Co<sub>9</sub>S<sub>8</sub>@carbon nanotubes on a carbon sheet: Facile controlled synthesis, and application to electrocatalysis in oxygen reduction/oxygen evolution reactions, and to a rechargeable Zn–air battery. *Inorg. Chem. Front.* **2021**, *8*, 368–375. [[CrossRef](#)]
46. Arafat, Y.; Azhar, M.R.; Zhong, Y.; Xu, X.; Tadé, M.O.; Shao, Z. A Porous nano-micro-composite as a high-performance bi-functional air electrode with remarkable stability for rechargeable Zinc–Air batteries. *Nano-Micro Lett.* **2020**, *12*, 130. [[CrossRef](#)]
47. Wang, X.; Ge, L.; Lu, Q.; Dai, J.; Guan, D.; Ran, R.; Weng, S.-C.; Hu, Z.; Zhou, W.; Shao, Z. High-performance metal-organic framework-perovskite hybrid as an important component of the air-electrode for rechargeable Zn–Air battery. *J. Power Sources* **2020**, *468*, 228377. [[CrossRef](#)]
48. Tan, J.; Thomas, T.; Liu, J.; Yang, L.; Pan, L.; Cao, R.; Shen, H.; Wang, J.; Liu, J.; Yang, M. Rapid microwave-assisted preparation of high-performance bifunctional Ni<sub>3</sub>Fe/Co–N–C for rechargeable Zn–air battery. *Chem. Eng. J.* **2020**, *395*, 125151. [[CrossRef](#)]
49. Chen, D.; Yu, J.; Cui, Z.; Zhang, Q.; Chen, X.; Sui, J.; Dong, H.; Yu, L.; Dong, L. Hierarchical architecture derived from two-dimensional zeolitic imidazolate frameworks as an efficient metal-based bifunctional oxygen electrocatalyst for rechargeable Zn–air batteries. *Electrochim. Acta* **2020**, *331*, 135394. [[CrossRef](#)]
50. Yu, N.-F.; Wu, C.; Huang, W.; Chen, Y.-H.; Ruan, D.-Q.; Bao, K.-L.; Chen, H.; Zhang, Y.; Zhu, Y.; Huang, Q.-H.; et al. Highly efficient Co<sub>3</sub>O<sub>4</sub>/Co@NCs bifunctional oxygen electrocatalysts for long life rechargeable Zn–air batteries. *Nano Energy* **2020**, *77*, 105200. [[CrossRef](#)]
51. Li, L.; Yang, J.; Yang, H.; Zhang, L.; Shao, J.; Huang, W.; Liu, B.; Dong, X. Anchoring Mn<sub>3</sub>O<sub>4</sub> Nanoparticles on oxygen functionalized carbon nanotubes as bifunctional catalyst for rechargeable zinc-air battery. *ACS Appl. Energy Mater.* **2018**, *1*, 963–969. [[CrossRef](#)]
52. Huang, Z.; Qin, X.; Gu, X.; Li, G.; Mu, Y.; Wang, N.; Ithisuphalap, K.; Wang, H.; Guo, Z.; Shi, Z.; et al. Mn<sub>3</sub>O<sub>4</sub> quantum dots supported on nitrogen-doped partially exfoliated multiwall carbon nanotubes as oxygen reduction electrocatalysts for high-performance Zn–Air batteries. *ACS Appl. Mater. Interfaces* **2018**, *10*, 23900–23909. [[CrossRef](#)]
53. Sidhureddy, B.; Prins, S.; Wen, J.; Thiruppathi, A.R.; Govindhan, M.; Chen, A. Synthesis and electrochemical study of mesoporous nickel-cobalt oxides for efficient oxygen reduction. *ACS Appl. Mater. Interfaces* **2019**, *11*, 18295–18304. [[CrossRef](#)] [[PubMed](#)]
54. Zhang, L.; Li, Y.; Peng, J.; Peng, K. Bifunctional NiCo<sub>2</sub>O<sub>4</sub> porous nanotubes electrocatalyst for overall water-splitting. *Electrochim. Acta* **2019**, *318*, 762–769. [[CrossRef](#)]
55. Dilshad, K.A.J.; Rabinal, M.K. Rationally designed Zn-anode and Co<sub>3</sub>O<sub>4</sub>-cathode nanoelectrocatalysts for an efficient Zn–air battery. *Energy Fuels* **2021**, *35*, 12588–12598. [[CrossRef](#)]
56. Worku, A.K.; Ayele, D.W.; Habtu, N.G.; Teshager, M.A.; Workineh, Z.G. Recent progress in MnO<sub>2</sub>-based oxygen electrocatalysts for rechargeable zinc-air batteries. *Mater. Today Sustain.* **2021**, *13*, 100072. [[CrossRef](#)]
57. Rittirum, M.; Buapin, P.; Saelee, T.; Khajondetchairit, P.; Kheawhom, S.; Alling, B.; Praserttham, S.; Ektarawong, A.; Praserttham, P. First-principles calculation on effects of oxygen vacancy on α-MnO<sub>2</sub> and β-MnO<sub>2</sub> during oxygen reduction reaction for rechargeable metal-air batteries. *J. Alloys Compd.* **2022**, *926*, 166929. [[CrossRef](#)]
58. Li, L.; Feng, X.; Nie, Y.; Chen, S.; Shi, F.; Xiong, K.; Ding, W.; Qi, X.; Hu, J.; Wei, Z.; et al. Insight into the effect of oxygen vacancy concentration on the catalytic performance of MnO<sub>2</sub>. *ACS Catal.* **2015**, *5*, 4825–4832. [[CrossRef](#)]

59. Gupta, P.K.; Bhandari, A.; Saha, S.; Bhattacharya, J.; Pala, R.G.S. Modulating oxygen evolution reactivity in MnO<sub>2</sub> through polymorphic engineering. *J. Phys. Chem. C* **2019**, *123*, 22345–22357. [CrossRef]
60. Zhou, Y.; Zhou, Z.; Hu, L.; Tian, R.; Wang, Y.; Arandiyani, H.; Chen, F.; Li, M.; Wan, T.; Han, Z.; et al. A facile approach to tailor electrocatalytic properties of MnO<sub>2</sub> through tuning phase transition, surface morphology and band structure. *Chem. Eng. J.* **2022**, *438*, 135561. [CrossRef]
61. Bera, K.; Karmakar, A.; Karthick, K.; Sankar, S.S.; Kumaravel, S.; Madhu, R.; Kundu, S. Enhancement of the OER kinetics of the less-explored  $\alpha$ -MnO<sub>2</sub> via nickel doping approaches in alkaline medium. *Inorg. Chem.* **2021**, *60*, 19429–19439. [CrossRef]
62. Ni, S.; Zhang, H.; Zhao, Y.; Li, X.; Sun, Y.; Qian, J.; Xu, Q.; Gao, P.; Wu, D.; Kato, K.; et al. Single atomic Ag enhances the bifunctional activity and cycling stability of MnO<sub>2</sub>. *Chem. Eng. J.* **2019**, *366*, 631–638. [CrossRef]
63. Zhang, J.-N. (Ed.) Carbon-Based Nanomaterials for Energy Conversion and Storage. In *Springer Series in Materials Science*; Springer Nature Singapore: Singapore, 2022; Volume 325, ISBN 978-981-19-4624-0.
64. Singh, B.; Gawande, M.B.; Kute, A.D.; Varma, R.S.; Fornasiero, P.; McNeice, P.; Jagadeesh, R.V.; Beller, M.; Zbořil, R. Single-atom (Iron-based) catalysts: Synthesis and applications. *Chem. Rev.* **2021**, *121*, 13620–13697. [CrossRef]
65. Global Industrial Catalyst Market Outlook to 2028. Available online: <https://www.researchandmarkets.com/reports/5778274/global-industrial-catalyst-market-outlook> (accessed on 11 July 2023).
66. Jiao, L.; Wan, G.; Zhang, R.; Zhou, H.; Yu, S.; Jiang, H. From Metal–organic frameworks to single-atom Fe implanted N-doped porous carbons: Efficient oxygen reduction in both alkaline and acidic media. *Angew. Chem. Int. Ed.* **2018**, *57*, 8525–8529. [CrossRef] [PubMed]
67. Yang, G.; Zhu, J.; Yuan, P.; Hu, Y.; Qu, G.; Lu, B.-A.; Xue, X.; Yin, H.; Cheng, W.; Cheng, J.; et al. Regulating Fe-spin state by atomically dispersed Mn-N in Fe-N-C catalysts with high oxygen reduction activity. *Nat. Commun.* **2021**, *12*, 1734. [CrossRef]
68. Mun, Y.; Lee, S.; Kim, K.; Kim, S.; Lee, S.; Han, J.W.; Lee, J. Versatile strategy for tuning ORR activity of a single Fe-N<sub>4</sub> site by controlling electron-withdrawing/donating properties of a carbon plane. *J. Am. Chem. Soc.* **2019**, *141*, 6254–6262. [CrossRef]
69. Liu, K.; Fu, J.; Lin, Y.; Luo, T.; Ni, G.; Li, H.; Lin, Z.; Liu, M. Insights into the activity of single-atom Fe-N-C catalysts for oxygen reduction reaction. *Nat. Commun.* **2022**, *13*, 2075. [CrossRef]
70. Shen, H.; Thomas, T.; Rasaki, S.A.; Saad, A.; Hu, C.; Wang, J.; Yang, M. Oxygen Reduction Reactions of Fe-N-C Catalysts: Current Status and the Way Forward. *Electrochem. Energy Rev.* **2019**, *2*, 252–276. [CrossRef]
71. Li, Y.; Xu, K.; Zhang, Q.; Zheng, Z.; Li, S.; Zhao, Q.; Li, C.; Dong, C.; Mei, Z.; Pan, F.; et al. One-pot synthesis of FeN<sub>x</sub>C as efficient catalyst for high-performance zinc-air battery. *J. Energy Chem.* **2022**, *66*, 100–106. [CrossRef]
72. Chen, Y.; Ji, S.; Chen, C.; Peng, Q.; Wang, D.; Li, Y. Single-atom catalysts: Synthetic strategies and electrochemical applications. *Joule* **2018**, *2*, 1242–1264. [CrossRef]
73. Jia, N.; Xu, Q.; Zhao, F.; Gao, H.-X.; Song, J.; Chen, P.; An, Z.; Chen, X.; Chen, Y. Fe/N Codoped Carbon nanocages with single-atom feature as efficient oxygen reduction reaction electrocatalyst. *ACS Appl. Energy Mater.* **2018**, *1*, 4982–4990. [CrossRef]
74. Ma, L.; Chen, S.; Pei, Z.; Huang, Y.; Liang, G.; Mo, F.; Yang, Q.; Su, J.; Gao, Y.; Zapien, J.A.; et al. Single-Site Active Iron-Based Bifunctional Oxygen Catalyst for a Compressible and Rechargeable Zinc–Air Battery. *ACS Nano* **2018**, *12*, 1949–1958. [CrossRef]
75. Yang, L.; Cheng, D.; Xu, H.; Zeng, X.; Wan, X.; Shui, J.; Xiang, Z.; Cao, D. Unveiling the high-activity origin of single-atom iron catalysts for oxygen reduction reaction. *Proc. Natl. Acad. Sci. USA* **2018**, *115*, 6626–6631. [CrossRef]
76. Zhang, L.; Liu, T.; Chen, N.; Jia, Y.; Cai, R.; Theis, W.; Yang, X.; Xia, Y.; Yang, D.; Yao, X. Scalable and controllable synthesis of atomic metal electrocatalysts assisted by an egg-box in alginate. *J. Mater. Chem. A* **2018**, *6*, 18417–18425. [CrossRef]
77. Lu, Z.; Wang, B.; Hu, Y.; Liu, W.; Zhao, Y.; Yang, R.; Li, Z.; Luo, J.; Chi, B.; Jiang, Z.; et al. An isolated zinc–cobalt atomic pair for highly active and durable oxygen reduction. *Angew. Chem.* **2019**, *131*, 2648–2652. [CrossRef]
78. Li, S.; Zhou, X.; Fang, G.; Xie, G.; Liu, X.; Lin, X.; Qiu, H.-J. Multicomponent spinel metal oxide nanocomposites as high-performance bifunctional catalysts in Zn–Air batteries. *ACS Appl. Energy Mater.* **2020**, *3*, 7710–7718. [CrossRef]
79. Zhang, B.; Zheng, X.; Voznyy, O.; Comin, R.; Bajdich, M.; García-Melchor, M.; Han, L.; Xu, J.; Liu, M.; Zheng, L.; et al. Homogeneously dispersed multimetal oxygen-evolving catalysts. *Science* **2016**, *352*, 333–337. [CrossRef]
80. Song, W.; Ren, Z.; Chen, S.-Y.; Meng, Y.; Biswas, S.; Nandi, P.; Elsen, H.A.; Gao, P.-X.; Suib, S.L. Ni- and Mn-promoted mesoporous Co<sub>3</sub>O<sub>4</sub>: A stable bifunctional catalyst with surface-structure-dependent activity for oxygen reduction reaction and oxygen evolution reaction. *ACS Appl. Mater. Interfaces* **2016**, *8*, 20802–20813. [CrossRef]
81. Liang, Y.; Wang, H.; Zhou, J.; Li, Y.; Wang, J.; Regier, T.; Dai, H. Covalent hybrid of spinel manganese–cobalt oxide and Graphene as advanced oxygen reduction electrocatalysts. *J. Am. Chem. Soc.* **2012**, *134*, 3517–3523. [CrossRef] [PubMed]
82. Xu, N.; Qiao, J.; Zhang, X.; Ma, C.; Jian, S.; Liu, Y.; Pei, P. Morphology controlled La<sub>2</sub>O<sub>3</sub>/Co<sub>3</sub>O<sub>4</sub>/MnO<sub>2</sub>–CNTs hybrid nanocomposites with durable bi-functional air electrode in high-performance zinc–air energy storage. *Appl. Energy* **2016**, *175*, 495–504. [CrossRef]
83. Xiao, X.; Hu, X.; Liang, Y.; Zhang, G.; Wang, X.; Yan, Y.; Li, X.; Yan, G.; Wang, J. Anchoring NiCo<sub>2</sub>O<sub>4</sub> nanowhiskers in biomass-derived porous carbon as superior oxygen electrocatalyst for rechargeable Zn–air battery. *J. Power Sources* **2020**, *476*, 228684. [CrossRef]
84. Go, Y.; Min, K.; An, H.; Kim, K.; Eun Shim, S.; Baeck, S.-H. Oxygen-vacancy-rich CoFe/CoFe<sub>2</sub>O<sub>4</sub> embedded in N-doped hollow carbon spheres as a highly efficient bifunctional electrocatalyst for Zn–air batteries. *Chem. Eng. J.* **2022**, *448*, 137665. [CrossRef]

85. Jose, V.; Hu, H.; Edison, E.; Manalastas, W.; Ren, H.; Kidkhunthod, P.; Sreejith, S.; Jayakumar, A.; Nsanzimana, J.M.V.; Srinivasan, M.; et al. Modulation of Single Atomic Co and Fe Sites on hollow carbon nanospheres as oxygen electrodes for rechargeable Zn–Air batteries. *Small Methods* **2021**, *5*, 2000751. [[CrossRef](#)]
86. Li, C.; Wu, M.; Liu, R. High-performance bifunctional oxygen electrocatalysts for zinc-air batteries over mesoporous Fe/Co-N-C nanofibers with embedding FeCo alloy nanoparticles. *Appl. Catal. B Environ.* **2019**, *244*, 150–158. [[CrossRef](#)]
87. Jia, X.; Zhao, Y.; Chen, G.; Shang, L.; Shi, R.; Kang, X.; Waterhouse, G.I.N.; Wu, L.-Z.; Tung, C.-H.; Zhang, T. Ni<sub>3</sub>FeN Nanoparticles Derived from Ultrathin NiFe-Layered Double Hydroxide Nanosheets: An efficient overall water splitting electrocatalyst. *Adv. Energy Mater.* **2016**, *6*, 1502585. [[CrossRef](#)]
88. Nørskov, J.K.; Rossmeisl, J.; Logadottir, A.; Lindqvist, L.; Kitchin, J.R.; Bligaard, T.; Jónsson, H. Origin of the overpotential for oxygen reduction at a fuel-cell cathode. *J. Phys. Chem. B* **2004**, *108*, 17886–17892. [[CrossRef](#)]
89. Jensen, K.D.; Tymoczko, J.; Rossmeisl, J.; Bandarenka, A.S.; Chorkendorff, I.; Escudero-Escribano, M.; Stephens, I.E.L. Elucidation of the oxygen reduction volcano in alkaline media using a copper-platinum (111) alloy. *Angew. Chem. Int. Ed.* **2018**, *57*, 2800–2805. [[CrossRef](#)]
90. Shao, M.; Chang, Q.; Dodelet, J.-P.; Chenitz, R. Recent Advances in electrocatalysts for oxygen reduction reaction. *Chem. Rev.* **2016**, *116*, 3594–3657. [[CrossRef](#)]
91. Nie, Y.; Li, L.; Wei, Z. Recent advancements in Pt and Pt-free catalysts for oxygen reduction reaction. *Chem. Soc. Rev.* **2015**, *44*, 2168–2201. [[CrossRef](#)] [[PubMed](#)]
92. Xiong, Y.; Shan, H.; Zhou, Z.; Yan, Y.; Chen, W.; Yang, Y.; Liu, Y.; Tian, H.; Wu, J.; Zhang, H.; et al. Tuning surface structure and strain in Pd-Pt core-shell nanocrystals for enhanced electrocatalytic oxygen reduction. *Small* **2017**, *13*, 1603423. [[CrossRef](#)] [[PubMed](#)]
93. Cui, Z.; Fu, G.; Li, Y.; Goodenough, J.B. Ni<sub>3</sub>FeN-Supported Fe<sub>3</sub>Pt intermetallic nanoalloy as a high-performance bifunctional catalyst for Metal–Air Batteries. *Angew. Chem. Int. Ed.* **2017**, *56*, 9901–9905. [[CrossRef](#)] [[PubMed](#)]
94. Liu, T.; Sun, F.; Huang, M.; Guan, L. Ternary PtZnCu Intermetallic Nanoparticles as an efficient oxygen reduction electrocatalyst for fuel cells with ultralow Pt loading. *ACS Appl. Energy Mater.* **2022**, *5*, 12219–12226. [[CrossRef](#)]
95. Lyu, X.; Zhang, W.; Liu, S.; Wang, X.; Li, G.; Shi, B.; Wang, K.; Wang, X.; Wang, Q.; Jia, Y. A magnetic field strategy to porous Pt-Ni nanoparticles with predominant (111) facets for enhanced electrocatalytic oxygen reduction. *J. Energy Chem.* **2021**, *53*, 192–196. [[CrossRef](#)]
96. Rossmeisl, J.; Karlberg, G.S.; Jaramillo, T.; Nørskov, J.K. Steady state oxygen reduction and cyclic voltammetry. *Faraday Discuss.* **2009**, *140*, 337–346. [[CrossRef](#)]
97. Rebrov, E.V.; Klinger, E.A.; Berenguer-Murcia, A.; Sulman, E.M.; Schouten, J.C. Selective hydrogenation of 2-Methyl-3-butyne-2-ol in a wall-coated capillary microreactor with a Pd<sub>25</sub>Zn<sub>75</sub>/TiO<sub>2</sub> Catalyst. *Org. Process Res. Dev.* **2009**, *13*, 991–998. [[CrossRef](#)]
98. Cherkasov, N.; Ibadon, A.O.; Rebrov, E.V. Novel synthesis of thick wall coatings of titania supported Bi poisoned Pd catalysts and application in selective hydrogenation of acetylene alcohols in capillary microreactors. *Lab Chip* **2015**, *15*, 1952–1960. [[CrossRef](#)]
99. Cui, Z.; Chen, H.; Zhao, M.; DiSalvo, F.J. High-Performance Pd<sub>3</sub>Pb Intermetallic Catalyst for Electrochemical Oxygen Reduction. *Nano Lett.* **2016**, *16*, 2560–2566. [[CrossRef](#)] [[PubMed](#)]
100. Slanac, D.A.; Hardin, W.G.; Johnston, K.P.; Stevenson, K.J. Atomic ensemble and electronic effects in Ag-rich AgPd nanoalloy catalysts for oxygen reduction in alkaline media. *J. Am. Chem. Soc.* **2012**, *134*, 9812–9819. [[CrossRef](#)]
101. Lüsi, M.; Erikson, H.; Merisalu, M.; Kasikov, A.; Matisen, L.; Sammelselg, V.; Tammeveski, K. Oxygen electroreduction in alkaline solution on Pd coatings prepared by galvanic exchange of copper. *Electrocatalysis* **2018**, *9*, 400–408. [[CrossRef](#)]
102. Betancourt, L.E.; Rojas-Pérez, A.; Orozco, I.; Frenkel, A.I.; Li, Y.; Sasaki, K.; Senanayake, S.D.; Cabrera, C.R. Enhancing ORR performance of bimetallic PdAg electrocatalysts by designing interactions between Pd and Ag. *ACS Appl. Energy Mater.* **2020**, *3*, 2342–2349. [[CrossRef](#)]
103. Biao, K.; Dongwei, L.; Yanjun, H.; Zeng, W.M. Au/Cu<sub>2</sub>O composite material, super-assembly preparation method and application. Patent No. CN113707890A, 17 August 2021.
104. Wang, Q.; O'Hare, D. Recent Advances in the synthesis and application of Layered Double Hydroxide (LDH) Nanosheets. *Chem. Rev.* **2012**, *112*, 4124–4155. [[CrossRef](#)] [[PubMed](#)]
105. Zhang, J.; Zhang, H.; Huang, Y. Electron-rich NiFe layered double hydroxides via interface engineering for boosting electrocatalytic oxygen evolution. *Appl. Catal. B Environ.* **2021**, *297*, 120453. [[CrossRef](#)]
106. Gao, R.; Yan, D. Recent Development of Ni/Fe-based micro/nanostructures toward Photo/Electrochemical water oxidation. *Adv. Energy Mater.* **2020**, *10*, 1900954. [[CrossRef](#)]
107. Zhang, H.; Li, H.; Akram, B.; Wang, X. Fabrication of NiFe layered double hydroxide with well-defined laminar superstructure as highly efficient oxygen evolution electrocatalysts. *Nano Res.* **2019**, *12*, 1327–1331. [[CrossRef](#)]
108. Xie, J.; Qu, H.; Lei, F.; Peng, X.; Liu, W.; Gao, L.; Hao, P.; Cui, G.; Tang, B. Partially amorphous nickel–iron layered double hydroxide nanosheet arrays for robust bifunctional electrocatalysis. *J. Mater. Chem. A* **2018**, *6*, 16121–16129. [[CrossRef](#)]
109. Zhao, D.; Jiang, K.; Pi, Y.; Huang, X. Superior Electrochemical Oxygen Evolution Enabled by Three-Dimensional Layered Double hydroxide nanosheet superstructures. *ChemCatChem* **2017**, *9*, 84–88. [[CrossRef](#)]
110. Li, K.; Guo, D.; Kang, J.; Wei, B.; Zhang, X.; Chen, Y. Hierarchical hollow spheres assembled with ultrathin CoMn double hydroxide nanosheets as trifunctional electrocatalyst for overall water splitting and Zn air battery. *ACS Sustain. Chem. Eng.* **2018**, *6*, 14641–14651. [[CrossRef](#)]

111. Guo, X.; Zheng, T.; Ji, G.; Hu, N.; Xu, C.; Zhang, Y. Core/shell design of efficient electrocatalysts based on NiCo<sub>2</sub>O<sub>4</sub> nanowires and NiMn LDH nanosheets for rechargeable zinc–air batteries. *J. Mater. Chem. A* **2018**, *6*, 10243–10252. [[CrossRef](#)]
112. Loizou, K.; Mourdikoudis, S.; Sergides, A.; Besenhard, M.O.; Sarafidis, C.; Higashimine, K.; Kalogirou, O.; Maenosono, S.; Thanh, N.T.K.; Gavriilidis, A. rapid millifluidic synthesis of stable high magnetic moment Fe<sub>x</sub>C<sub>y</sub> nanoparticles for hyperthermia. *ACS Appl. Mater. Interfaces* **2020**, *12*, 28520–28531. [[CrossRef](#)] [[PubMed](#)]
113. Rebrov, E.V.; Gao, P.; Verhoeven, T.M.W.G.M.; Schouten, J.C.; Kleismit, R.; Turgut, Z.; Kozłowski, G. Structural and magnetic properties of sol–gel Co<sub>2x</sub>Ni<sub>0.5–x</sub>Zn<sub>0.5–x</sub>Fe<sub>2</sub>O<sub>4</sub> thin films. *J. Magn. Magn. Mater.* **2011**, *323*, 723–729. [[CrossRef](#)]
114. Houlding, T.K.; Gao, P.; Degirmenci, V.; Tchabanenko, K.; Rebrov, E.V. Mechanochemical synthesis of TiO<sub>2</sub>/NiFe<sub>2</sub>O<sub>4</sub> magnetic catalysts for operation under RF field. *Mater. Sci. Eng. B* **2015**, *193*, 175–180. [[CrossRef](#)]
115. Yan, B.; Gao, P.; Lu, Z.; Ma, R.; Rebrov, E.V.; Zheng, H.; Gao, Y. Effect of Pr<sup>3+</sup> substitution on the microstructure, specific surface area, magnetic properties and specific heating rate of Ni<sub>0.5</sub>Zn<sub>0.5</sub>Pr<sub>x</sub>Fe<sub>2–x</sub>O<sub>4</sub> nanoparticles synthesized via sol–gel method. *J. Alloys Compd.* **2015**, *639*, 626–634. [[CrossRef](#)]
116. Houlding, T.K.; Rebrov, E.V. Application of alternative energy forms in catalytic reactor engineering. *Green Process. Synth.* **2012**, *1*, 19–31. [[CrossRef](#)]
117. Liu, H.; Ren, Y.; Wang, K.; Mu, X.; Song, S.; Guo, J.; Yang, X.; Lu, Z. Magnetic-field-induced strain enhances electrocatalysis of FeCo alloys on anode catalysts for water splitting. *Metals* **2022**, *12*, 800. [[CrossRef](#)]
118. Zeng, Z.; Zhang, T.; Liu, Y.; Zhang, W.; Yin, Z.; Ji, Z.; Wei, J. Magnetic field-enhanced 4-electron pathway for well-aligned Co<sub>3</sub>O<sub>4</sub> /electrospun carbon nanofibers in the oxygen reduction reaction. *ChemSusChem* **2018**, *11*, 580–588. [[CrossRef](#)] [[PubMed](#)]
119. Li, Y.; Zhang, L.; Peng, J.; Zhang, W.; Peng, K. Magnetic field enhancing electrocatalysis of Co<sub>3</sub>O<sub>4</sub>/NF for oxygen evolution reaction. *J. Power Sources* **2019**, *433*, 226704. [[CrossRef](#)]
120. Li, X.; Cheng, Z.; Wang, X. Understanding the mechanism of the oxygen evolution reaction with consideration of spin. *Electrochem. Energy Rev.* **2021**, *4*, 136–145. [[CrossRef](#)]
121. Zhang, Y.; Guo, P.; Li, S.; Sun, J.; Wang, W.; Song, B.; Yang, X.; Wang, X.; Jiang, Z.; Wu, G.; et al. Magnetic field assisted electrocatalytic oxygen evolution reaction of nickel-based materials. *J. Mater. Chem. A* **2022**, *10*, 1760–1767. [[CrossRef](#)]
122. Zheng, H.; Wang, Y.; Xie, J.; Gao, P.; Li, D.; Rebrov, E.V.; Qin, H.; Liu, X.; Xiao, H. Enhanced alkaline oxygen evolution using spin polarization and magnetic heating effects under an AC magnetic field. *ACS Appl. Mater. Interfaces* **2022**, *14*, 34627–34636. [[CrossRef](#)]
123. Chen, H.; Zheng, H.; Yang, T.; Yue, S.; Gao, P.; Liu, X.; Xiao, H. AC magnetic field enhancement oxygen evolution reaction of bimetallic metal-organic framework. *Int. J. Hydrogen Energy* **2022**, *47*, 18675–18687. [[CrossRef](#)]
124. Wu, T.; Xu, Z.J. Oxygen evolution in spin-sensitive pathways. *Curr. Opin. Electrochem.* **2021**, *30*, 100804. [[CrossRef](#)]
125. Wu, T.; Ren, X.; Sun, Y.; Sun, S.; Xian, G.; Scherer, G.G.; Fisher, A.C.; Mandler, D.; Ager, J.W.; Grimaud, A.; et al. Spin pinning effect to reconstructed oxyhydroxide layer on ferromagnetic oxides for enhanced water oxidation. *Nat. Commun.* **2021**, *12*, 3634. [[CrossRef](#)]
126. Zheng, H.; Chen, H.; Wang, Y.; Gao, P.; Liu, X.; Rebrov, E.V. Fabrication of magnetic superstructure NiFe<sub>2</sub>O<sub>4</sub> @MOF-74 and its derivative for electrocatalytic hydrogen evolution with AC magnetic field. *ACS Appl. Mater. Interfaces* **2020**, *12*, 45987–45996. [[CrossRef](#)] [[PubMed](#)]
127. Wang, Y.; Yang, T.; Yue, S.; Zheng, H.; Liu, X.; Gao, P.; Qin, H.; Xiao, H. Effects of alternating magnetic fields on the OER of heterogeneous core–shell structured NiFe<sub>2</sub>O<sub>4</sub>/(Ni,Fe)S/P. *ACS Appl. Mater. Interfaces* **2023**, *15*, 11631–11641. [[CrossRef](#)]
128. Wang, K.; Yang, Q.; Zhang, H.; Zhang, M.; Jiang, H.; Zheng, C.; Li, J. Recent advances in catalyst design and activity enhancement induced by a magnetic field for electrocatalysis. *J. Mater. Chem. A* **2023**, *11*, 7802–7832. [[CrossRef](#)]
129. Sun, Z.; Lin, L.; He, J.; Ding, D.; Wang, T.; Li, J.; Li, M.; Liu, Y.; Li, Y.; Yuan, M.; et al. Regulating the Spin State of Fe III Enhances the Magnetic Effect of the Molecular Catalysis Mechanism. *J. Am. Chem. Soc.* **2022**, *144*, 8204–8213. [[CrossRef](#)] [[PubMed](#)]
130. Ge, J.; Chen, R.R.; Ren, X.; Liu, J.; Ong, S.J.H.; Xu, Z.J. Ferromagnetic–antiferromagnetic coupling core–shell nanoparticles with spin conservation for water oxidation. *Adv. Mater.* **2021**, *33*, 2101091. [[CrossRef](#)] [[PubMed](#)]
131. Gong, X.; Jiang, Z.; Zeng, W.; Hu, C.; Luo, X.; Lei, W.; Yuan, C. Alternating magnetic field induced magnetic heating in ferromagnetic cobalt Single-Atom Catalysts for efficient oxygen evolution reaction. *Nano Lett.* **2022**, *22*, 9411–9417. [[CrossRef](#)]
132. Niether, C.; Faure, S.; Bordet, A.; Deseure, J.; Chatenet, M.; Carrey, J.; Chaudret, B.; Rouet, A. Improved water electrolysis using magnetic heating of FeC–Ni core–shell nanoparticles. *Nat. Energy* **2018**, *3*, 476–483. [[CrossRef](#)]
133. Peng, D.; Hu, C.; Luo, X.; Huang, J.; Ding, Y.; Zhou, W.; Zhou, H.; Yang, Y.; Yu, T.; Lei, W.; et al. Electrochemical reconstruction of NiFe/NiFeOOH superparamagnetic core/catalytic shell heterostructure for magnetic heating enhancement of oxygen evolution reaction. *Small* **2023**, *19*, 2205665. [[CrossRef](#)] [[PubMed](#)]
134. Deng, J.; Qiao, H.; Li, C.; Huang, Z.; Luo, S.; Qi, X. Magnetic field enhanced surface activity of ferromagnetic Cr<sub>2</sub>Ge<sub>2</sub>Te<sub>6</sub> nanosheets for electrocatalytic oxygen evolution reaction. *Appl. Surf. Sci.* **2023**, *637*, 157899. [[CrossRef](#)]
135. Su, M.; Zhou, W.; Liu, L.; Chen, M.; Jiang, Z.; Luo, X.; Yang, Y.; Yu, T.; Lei, W.; Yuan, C. Micro eddy current facilitated by screwed MoS<sub>2</sub> structure for enhanced hydrogen evolution reaction. *Adv. Funct. Mater.* **2022**, *32*, 2111067. [[CrossRef](#)]

**Disclaimer/Publisher’s Note:** The statements, opinions and data contained in all publications are solely those of the individual author(s) and contributor(s) and not of MDPI and/or the editor(s). MDPI and/or the editor(s) disclaim responsibility for any injury to people or property resulting from any ideas, methods, instructions or products referred to in the content.